Monthly Notices
of the
ROYAL ASTRONOMICAL SOCIETY

MNRAS **456,** 2105–2125 (2016) doi:10.1093/mnras/stv2748

Mid-infrared luminous quasars in the GOODS–*Herschel* fields: a large population of heavily obscured, Compton-thick quasars at $z \approx 2$

A. Del Moro,[1,2⋆] D. M. Alexander,[1] F. E. Bauer,[3,4,5,6] E. Daddi,[7] D. D. Kocevski,[8] D. H. McIntosh,[9] F. Stanley,[1] W. N. Brandt,[10,11,12] D. Elbaz,[7] C. M. Harrison,[1] B. Luo,[13] J. R. Mullaney[14] and Y. Q. Xue[15]

[1]*Centre for Extragalactic Astronomy, Department of Physics, Durham University, South Road, Durham DH1 3LE, UK*
[2]*Max-Planck-Institut für Extraterrestrische Physik (MPE), Postfach 1312, D-85741 Garching, Germany*
[3]*Instituto de Astrofísica, Facultad de Física, Pontificia Universidad Católica de Chile, 306, Santiago 22, Chile*
[4]*Millenium Institute of Astrophysics, Vicuña Mackenna 4860, 7820436 Macul, Santiago, Chile*
[5]*EMBIGGEN Anillo, Concepción, Chile*
[6]*Space Science Institute, 4750 Walnut Street, Suite 205, Boulder, CO 80301, USA*
[7]*CEA-Saclay, F-91191 Gif-sur-Yvette Cedex, France*
[8]*Department of Physics and Astronomy, University of Kentucky, Lexington, KY 40506-0055, USA*
[9]*Department of Physics & Astronomy, University of Missouri-Kansas City, 5110 Rockhill Rd, Kansas City, MO 64110, USA*
[10]*Department of Astronomy and Astrophysics, 525 Davey Lab, Pennsylvania State University, University Park, PA 16802, USA*
[11]*Institute for Gravitation and the Cosmos, Pennsylvania State University, University Park, PA 16802, USA*
[12]*Department of Physics, Pennsylvania State University, University Park, PA 16802, USA*
[13]*School of Astronomy and Space Science, Nanjing University, Nanjing 210093, China*
[14]*Department of Physics and Astronomy, University of Sheffield, Hounsfield Road, Sheffield S3 7RH, UK*
[15]*Key Laboratory for Research in Galaxies and Cosmology, Department of Astronomy, University of Science and Technology of China, Chinese Academy of Sciences, Hefei, Anhui 230026, China*

Accepted 2015 November 19. Received 2015 November 19; in original form 2015 April 2

ABSTRACT

We present the infrared (IR) and X-ray properties of a sample of 33 mid-IR luminous quasars ($\nu L_{6\,\mu m} \geq 6 \times 10^{44}$ erg s^{-1}) at redshift $z \approx$ 1–3, identified through detailed spectral energy distribution analyses of distant star-forming galaxies, using the deepest IR data from *Spitzer* and *Herschel* in the GOODS–*Herschel* fields. The aim is to constrain the fraction of obscured, and Compton-thick (CT, $N_{\rm H} > 1.5 \times 10^{24}$ cm^{-2}) quasars at the peak era of nuclear and star formation activities. Despite being very bright in the mid-IR band, ≈30 per cent of these quasars are not detected in the extremely deep 2 and 4 Ms *Chandra* X-ray data available in these fields. X-ray spectral analysis of the detected sources reveals that the majority (≈67 per cent) are obscured by column densities $N_{\rm H} > 10^{22}$ cm^{-2}; this fraction reaches ≈80 per cent when including the X-ray-undetected sources (9 out of 33), which are likely to be the most heavily obscured, CT quasars. We constrain the fraction of CT quasars in our sample to be ≈24–48 per cent, and their space density to be $\Phi = (6.7 \pm 2.2) \times 10^{-6}$ Mpc^{-3}. From the investigation of the quasar host galaxies in terms of star formation rates (SFRs) and morphological distortions, as a sign of galaxy mergers/interactions, we do not find any direct relation between SFRs and quasar luminosity or X-ray obscuration. On the other hand, there is tentative evidence that the most heavily obscured quasars have, on average, more disturbed morphologies than the unobscured/moderately obscured quasar hosts, which preferentially live in undisturbed systems. However, the fraction of quasars with disturbed morphology amongst the whole sample is ≈40 per cent, suggesting that galaxy mergers are not the main fuelling mechanism of quasars at $z \approx 2$.

Key words: galaxies: active – quasars: general – galaxies: star formation – infrared: galaxies – X-rays: galaxies.

1 INTRODUCTION

Since the discovery that most, if not all, galaxy spheroids in the local Universe host a supermassive black hole (SMBH) whose mass

⋆ E-mail: adelmoro@mpe.mpg.de

scales with that of the host-galaxy bulge (e.g. Magorrian et al. 1998; Ferrarese & Merritt 2000; Marconi & Hunt 2003) it has been clear that there is likely to be a tight connection between the evolution of SMBHs and galaxies. Studies of the galaxy population across cosmic time have shown that galaxies were more actively growing in the past, as the star formation rate (SFR) density peaks at redshift $z \approx 2$ and rapidly declines to the present day (e.g. Madau et al. 1996; Hopkins et al. 2006). A similar evolution is seen in the moderate-to-high luminosity active galactic nucleus (AGN) population, where most of the SMBHs accrete more rapidly at high redshift ($z \gtrsim 1$–2), becoming more quiescent at $z = 0$ (e.g. Brandt & Alexander 2015, and references therein). Whether this parallel evolution between galaxies and SMBHs is simply due to a larger gas supply to feed both black hole accretion and star formation (SF) at high redshift, or whether there are other processes that self-regulate the SMBH and galaxy growth is still uncertain (e.g. Alexander & Hickox 2012; Kormendy & Ho 2013). A complete census of AGN is crucial to fully understand the accretion history of the SMBHs and their role in galaxy evolution. However, as the Universe at high redshift is more gas and dust rich, most of the accretion on to SMBHs is expected to be heavily obscured, which makes the identification and study of a large fraction of the AGN population very challenging.

X-ray observations provide arguably the most efficient way to trace the growth of SMBHs, as the high-energy radiation can penetrate large amounts of gas and dust without significant absorption. Moreover, the contamination from galaxy emission at X-ray energies is small as galaxies are typically much fainter than AGN in this band. However, when the column density of the obscuring material becomes Compton thick (CT; $N_{\rm H} > 1.5 \times 10^{24}$ cm^{-2}) even the deepest X-ray surveys often fail to detect the population of the most obscured, CT AGN (e.g. Xue et al. 2012; see Brandt & Alexander 2015 for a review). A significant fraction of such AGN is predicted by all models of the cosmic X-ray background (CXB) to reproduce the observed background spectrum at high energies ($E \approx 30$ keV; e.g. Comastri et al. 1995; Gilli, Comastri & Hasinger 2007; Treister, Urry & Virani 2009), however, the actual contribution from CT AGN is not well constrained and varies between the models, due to different assumptions, and the space density of CT AGN is still uncertain.

Since most of the absorbed AGN emission is re-emitted in the mid-infrared band (MIR; $\lambda \approx 3$–40 μm) by the circumnuclear dust heated by the central SMBH, observations in this band can potentially identify the elusive CT AGN missed by X-ray surveys (e.g. Lacy et al. 2004; Stern et al. 2005; Alexander et al. 2008; Donley et al. 2008, 2012; Fiore et al. 2008; Georgantopoulos et al. 2011a; Mateos et al. 2013). Moreover, since the infrared (IR) band is much less affected by extinction than the UV, optical and soft X-ray bands, the selection of AGN in the MIR band is almost unbiased against obscured AGN. The downside of using the IR band to study AGN is the strong contamination from SF in the host galaxies, whose cold dust emission tends to dominate the MIR to far-IR (FIR, $\lambda \approx$ 40–250 μm) bands, peaking at $\lambda \approx 100$–160 μm. This is especially the case for low-to-moderate luminosity AGN, whose IR emission is often swamped by SF. These sources are easily missed by typical MIR colour–colour sample selection, which are generally used to identify AGN within the star-forming galaxy (SFG) population (e.g. Lacy et al. 2004; Stern et al. 2005; Donley et al. 2012; Mateos et al. 2013).

In this paper, we investigate a sample of MIR luminous quasars (hereafter, 'IR quasars') at redshift $z \approx 1$–3, i.e. at the peak era of AGN and SF activity. We used the deepest available *Spitzer* and *Herschel* data in the GOODS–*Herschel* North and South fields (hereafter, GH-N and GH-S, respectively; Elbaz et al. 2011) to reliably identify AGN in the MIR band through detailed spectral energy distribution (SED) analyses, which allow us to disentangle the AGN and SF emissions at MIR and FIR wavelengths. The SED analysis is a much more powerful tool than the simple IR colour–colour techniques for identifying AGN, as it can recover the hot dust emission from the AGN even when it does not strongly dominate the SED (e.g. Del Moro et al. 2013; Rovilos et al. 2014); however even the SED analyses have limitations and become incomplete when the AGN component is faint compared to the SF component. Using the deepest *Chandra* X-ray data available across the sky (2 Ms in CDF-N; Alexander et al. 2003; and 4 Ms in CDF-S; Xue et al. 2011), we investigate the X-ray spectra of the IR quasars to constrain the fraction of obscured and CT sources. We also investigate the properties of their host galaxies to place them in the context of potential SMBH-galaxy evolution scenarios. The paper is organized as follows: in Section 2 the data used in our analyses are described, while Section 3 details the SED analysis method and the selection of our IR quasar sample. Section 4 presents the X-ray spectral analysis and results for our quasars, as well as the properties of their host galaxies assessed by the SFRs derived from our SED analyses, and their morphologies, obtained from visual classification of *HST*-WFC3 *K*-band images. In Section 5, the results obtained from our analyses are discussed in the wider context of the CXB models and the SMBH-galaxy evolutionary scenario. A summary and final remarks are given in Section 6. Throughout the paper we assume a cosmological model with $H_0 = 70$ km s^{-1} Mpc^{-1}, $\Omega_{\rm M} = 0.27$ and $\Omega_\Lambda = 0.73$ (Spergel et al. 2003). All the errors are quoted at a 90 per cent confidence level, unless otherwise stated.

2 DATA

2.1 IR observations

The GOODS fields have been observed in the IR band by the *Spitzer* and *Herschel* space observatories, and include the deepest IR data currently available. The *Spitzer* observations (Giavalisco et al. 2004) cover the MIR band at 3.6, 4.5, 5.8 and 8.0 μm with IRAC (Fazio et al. 2004) and at 24 μm with MIPS (Rieke et al. 2004) as part of the GOODS Legacy programme (PI: M. Dickinson). The 24 μm source catalogue was created using a point spread function (PSF) fitting technique at the 3.6 μm source positions as priors ($>5\sigma$ detections). For details of the observations and catalogue, we refer to Magnelli et al. (2009, 2011). In both fields, the 24 μm observations reach a point source sensitivity limit of ∼30 μJy (5σ).

FIR observations of the GOODS fields were undertaken by *Herschel* as part of the GOODS–*Herschel* survey project (GH; Elbaz et al. 2011). The GH survey covers the full ≈10 arcmin ×16 arcmin GOODS-N field with PACS (Poglitsch et al. 2008) at 100 and 160 μm and with SPIRE (Griffin et al. 2010) at 250, 350, 500 μm, for a total observing time of 124 h. In GOODS-S a smaller region of ≈10 arcmin ×10 arcmin at the centre of the field was observed by PACS at 100 and 160 μm and the total exposure was 206.3 h (GH-S; Elbaz et al. 2011). We also used the SPIRE 250 μm data observed as part of the *Herschel* Multi-tiered Extragalactic Survey (Oliver et al. 2012) across the GH-S field, to better match the data available in GH-N. We note that since the SPIRE data suffer from significant flux blending issues, we limit our analyses to the 250 μm band in both the GH-N and GH-S fields, where these issues can still be corrected fairly well.

The *Spitzer*-MIPS 24 μm source positions were used as priors to estimate the *Herschel* 100 μm, 160 μm and 250 μm fluxes through

PSF fitting (courtesy of E. Daddi). In the GH-N field 819 sources (∼42 per cent of the 24 μm priors) are detected in at least one of the *Herschel* bands down to 5σ (3σ) sensitivity limits of ∼1.7 (∼1.2) mJy, ∼4.5 (∼2.3) mJy and ∼6.5 (∼4.0) mJy, respectively. In the GH-S field there are 591 sources (∼34 per cent of the 24 μm priors) detected by *Herschel* (at 100, 160 or 250 μm); the faintest sources are detected down to 5σ (3σ) flux densities of 1.3 (0.7), 2.7 (1.7), 7.7 (5.0) mJy in the three bands, respectively; however, for general sources the flux densities and errors are higher, depending on the local source density and the de-blending uncertainties. In case of non-detection in any of the *Herschel* bands, appropriate flux density upper limits were calculated for each prior position.

In our analyses we initially considered all the 24 μm-detected sources within the GH fields, namely 1943 sources in GH-N and 1747 sources in GH-S (for a total of 3690 sources), with or without a *Herschel* detection. For the sample in GH-N ≈98 per cent of the sources have a redshift identification, of which ≈63 per cent are spectroscopic redshifts, while the remaining are photometric (see Del Moro et al. 2013, hereafter DM13, for a detailed description of the redshift compilation). In the GH-S field, a redshift identification is available for ≈86 per cent of the sources, of which ≈95 per cent are spectroscopic redshifts compiled from multiple catalogues available in the literature (Le Fèvre et al. 2004; Mignoli et al. 2005; Vanzella et al. 2008; Popesso et al. 2009; Balestra et al. 2010; Silverman et al. 2010; Xia et al. 2011) and 5 per cent are photometric redshifts.

2.2 X-ray observations

The X-ray counterparts for the 24 μm-detected sources in GH-N and GH-S were found by cross-matching the 24 μm positions with the X-ray source catalogues by Alexander et al. (2003) in the *Chandra* Deep Field North (CDF-N), constructed from the 2 Ms *Chandra* observations covering an area of ∼448 arcmin^2 of the sky, and by Xue et al. (2011) in the *Chandra* Deep Field South (CDF-S), from the 4 Ms *Chandra* data over a region of 464.5 arcmin^2. The CDF-N catalogue contains 503 X-ray-detected sources, down to flux limits of $f_{0.5-2\ \mathrm{keV}} \approx 2.5 \times 10^{-17}$ erg cm^{-2} s^{-1} and $f_{2-8\ \mathrm{keV}} \approx 1.4 \times 10^{-16}$ erg cm^{-2} s^{-1}. The CDF-S X-ray source catalogue contains 740 sources down to flux limits of $f_{0.5-2\ \mathrm{keV}} \approx 9.1 \times 10^{-18}$ erg cm^{-2} s^{-1} and $f_{2-8\ \mathrm{keV}} \approx 5.5 \times 10^{-17}$ erg cm^{-2} s^{-1}. For details on the data reduction and the construction of the catalogues we refer to Alexander et al. (2003), Luo et al. (2008) and Xue et al. (2011).

For the X-ray-detected sources in our sample (see Section 3.2), X-ray spectra have been extracted and analysed. The data were processed using the *Chandra* Interactive Analysis of Observations[1] (CIAO; version 4.3 and CALDB 4.4.1; Fruscione et al. 2006) tools and the ACIS Extract (AE) software package[2] (Broos et al. 2010, 2012). The *Chandra* spectra were produced using the AE software (version 2011-03-16), extracting source and background spectra in each individual observation, as well as the relative response matrices and ancillary files, and combining them using the FTOOLS[3] `addrmf` and `addarf` (Blackburn 1995).

[1] http://cxc.cfa.harvard.edu/ciao/index.html

[2] The ACIS Extract software package and users guide are available at http://www.astro.psu.edu/xray/acis/acis_analysis.html.

[3] http://heasarc.gsfc.nasa.gov/ftools/

2.3 Optical/near-infrared observations

The GOODS-N and GOODS-S fields have been observed by the *Hubble Space telescope* (*HST*) ACS camera as part of the GOODS project (Giavalisco et al. 2004), and WFC3 camera as part of the Cosmic Near-Infrared Deep Extragalactic Legacy Survey (CANDELS), a large programme consisting of broad-band photometric UV to the near-IR imaging of five separate deep extragalactic fields (see Grogin et al. 2011 and Koekemoer et al. 2011, for details on the observations and data reduction). The CANDELS *HST* observations in the GOODS-N field cover an area of ≈10 arcmin × 16 arcmin (CANDELS-Wide) with a deeper smaller region in the centre (CANDELS-DEEP; ≈6.8 arcmin × 10 arcmin). The imaging of the GOODS-S field covers a similar region as in GOODS-N, but also includes a small ultradeep area in the centre of the field (*Hubble* Ultra-Deep field; 2 arcmin × 2.3 arcmin). In this paper we mainly use data in the *F*125*W* and *F*160*W* bands, which approximately correspond to near-IR *J* and *H* bands, but also consider data from the optical *F*606*W* and *F*850*LP* bands (corresponding to the *V* and *z* bands, respectively), to corroborate our visual classification of the galaxy morphology (Section 4.4).

3 SED AND SAMPLE SELECTION

3.1 IR SED decomposition

To constrain the IR emission from the AGN and the host galaxies, our SED-fitting approach uses an empirical AGN template and five different SFG templates from Mullaney et al. (2011), which have been extended down to 3 μm and to the radio band (DM13). The AGN template at $\lambda \lesssim 40$ μm is represented by a broken power law, where the indices have been fixed at the average values of $\Gamma_1 = 1.7$ and $\Gamma_2 = 0.7$ and the power-law break at $\lambda = 19$ μm.[4] An extinction law (Draine 2003) is also applied to the AGN template, with the extinction parameter A_V free to vary in the range of $A_V = 0$–30 mag (Mullaney et al. 2011; DM13). The *Spitzer* 8, 16 and 24 μm and the *Herschel* 100, 160 and 250 μm photometric points are used to constrain the source SEDs (see Figs A1 and A2 in appendix); the *Spitzer* IRAC flux densities at 3.6, 4.5 and 5.8 μm are not included in the SED analysis because these data are likely to be dominated by starlight emission, which is not taken into account in our templates.

The SEDs for all of the 24 μm-detected sources with redshift measurements in the GH-N and GH-S fields have been initially fitted with the SFG templates only, and subsequently with the AGN + SFG templates obtaining a best-fitting solution for each of the SFG templates, using a χ^2-fitting technique (see DM13, for details). We adopted the Bayesian information criterion (BIC; Schwarz 1978) to assess the improvement of the fits due to the addition of the AGN component to each of the SFG templates, and therefore to identify the best-fitting model for each source. Namely, the AGN + SFG model is assumed as the best-fitting model if for each source:

[4] We also performed the SED fitting using Γ_1 as a free parameter for the sources with enough data points in the MIR band to constrain the power-law slope. We note that this is not the case for all the sources, as at $z \gtrsim 1.7$ the 8 μm data point falls out of the wavelength range covered by our SED templates. Moreover, in some cases the 16 μm data are upper limits and therefore cannot provide strong constraints to the MIR power-law slope. However, where the fits with Γ_1 as free parameter provided a better representation of the data compared to a fixed $\Gamma_1 = 1.7$, we adopted these fits as the best-fitting solutions.

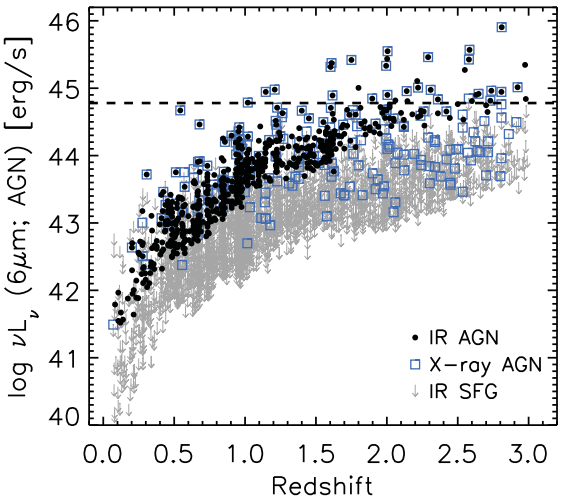

Figure 1. Rest-frame 6 μm AGN luminosity, calculated from the SED fits, versus redshift for all of the 24 μm-detected sources in the GH fields (∼3200 sources with $z \leq 3$, out of the total 3690 24 μm-detected sources). The black circles represent the sources where we significantly identify an AGN component in the IR SED (Section 3.1), while the blue open squares represent the X-ray-detected AGN. For sources where an AGN component was not found in the best-fitting SEDs ('IR SFG'), the 6 μm AGN luminosity is plotted as an upper limit (grey arrows). The dashed line at $\log \nu L_{6\,\mu m} = 44.78$ erg s^{-1} marks our threshold for the IR quasar selection.

(1) $\Delta BIC_i = BIC_{SFG,i} - BIC_{AGN+SFG,i} > 2$ (e.g. Kass & Raftery 1995), where $i = 1$–5 refers to each of the SFG templates, in at least 4 out of the 5 pairs of best-fitting solutions;

(2) $\min(\chi^2_{AGN+SFG,j}) < \min(\chi^2_{SFG,i})$, with $j \leq i$, i.e. the minimum χ^2 of the AGN + SFG solutions that satisfy condition (1) should be less than the minimum χ^2 obtained by fitting any of the SFG templates alone.

If any of these criteria is not met we conservatively adopt the simple SFG model as the best-fitting model. These criteria are adopted to assess the reliability of the AGN component independently from the individual SFG templates. In fact, due to the sparse data points available for our SED analysis, in some cases, individual fitting solutions from different templates yield similarly good fit to the data, preventing us from identifying a unique best-fitting solution. We refer to section 3.1 and appendix A of DM13, for a detailed description of the SED-fitting approach and tests on its reliability.[5]

After identifying the best-fitting model, we derived the luminosity of the AGN (i.e. corrected for the galaxy contribution) at rest-frame 6 μm ($L_{6\,\mu m,\ AGN}$), the IR luminosity of the AGN (L_{AGN}) calculated across the wavelength range $\lambda = 8$–1000 μm, and the IR luminosity of the SFG ($\lambda = 8$–1000 μm; hereafter L_{SF}), as weighted means of the values obtained from the five best-fitting model solutions [or from all the solutions satisfying condition (1) for the AGN + SFG model]. Where the AGN component was not significantly identified an upper limit to the AGN luminosity at 6 μm was set as 50 per cent of the total 6 μm emission (Fig. 1), i.e. the limit for the SFG component becoming dominant at 6 μm. For the cases where the FIR data (100, 160 and 250 μm) are all upper limits and our SED-fitting approach did not provide a reliable measurement of the SF emission, we estimated an upper limit for L_{SF} by increasing the normalization of the SFG templates until they reached any of the FIR upper limits, without exceeding any of the MIR data point measurements (including errors). An IR luminosity was calculated from each of the five templates and the highest value was then taken as the L_{SF} upper limit.

[5] We note that here we have slightly modified the criteria to evaluate the reliability of the AGN component compared to those presented in DM13, by adopting the BIC instead of an *f*-test. The BIC is a more appropriate statistical criterion to compare the results from different models than the *f*-test when the models are non-nested.

3.2 IR quasar sample

From the results obtained from our SED decomposition, we selected a sample of luminous AGN with $\nu L_{6\,\mu m,\ AGN} \geq 6 \times 10^{44}$ erg s^{-1}($\geq$ 44.78 in the logarithmic scale; Fig. 1), defined hereafter as our 'IR quasar' sample. Considering the intrinsic relation between the 6 μm luminosity and the X-ray luminosity observed for unobscured AGN (e.g. Lutz et al. 2004; Fiore et al. 2009; Gandhi et al. 2009; Mateos et al. 2015), our 6 μm luminosity cut corresponds to an intrinsic X-ray luminosity $L_{2-10\ keV} \approx 2.5 \times 10^{44}$ erg s^{-1}, i.e. clearly in the quasar regime even allowing for the ≈0.4 dex scatter in the relation. We also restricted our sample to the redshift range $z = 1$–3 as we aim to investigate the population of luminous quasars at the peak of activity at $z \approx 2$ (Madau et al. 1996; Hopkins et al. 2006; Ueda et al. 2014; Brandt & Alexander 2015). Our sample consists of 33 sources, 19 in the GH-N and 14 in the GH-S fields (see Table 1). The bolometric luminosities (L_{bol}) of these quasars, estimated as $L_{bol} \approx 2 \times L_{AGN}$ (assuming a bolometric correction of a factor of ∼8 at 6 μm, from Richards et al. 2006, and considering the median ratio of ∼0.3 between $\nu L_{6\,\mu m,\ AGN}$ and L_{AGN} estimated for our quasars), span the range $\log L_{bol} = 45.4$–46.5 erg s^{-1} (see Table 1). For all of these sources, we find that the AGN component largely dominates over the SF component at MIR wavelengths, with the AGN contributing >66 per cent to the total emission at 6 μm ($f_{AGN} = 66$–100 per cent; where f_{AGN} is defined as the fraction of AGN luminosity over the total at rest-frame 6 μm; see Table 1). The best-fitting SEDs are reported in Appendix A (Figs A1 and A2). We note that for 13 out of the 33 sources (≈40 per cent) *Spitzer*-IRS low-resolution spectroscopy is available ($\lambda \approx 3$–20 μm; Pope et al. 2008a; Murphy et al. 2009; Kirkpatrick et al. 2012). Although we do not use these spectra to constrain the source SEDs, we find very good agreement between our SED best-fitting solutions and the *Spitzer*-IRS spectra, which are shown in Figs A1 and A2 (Appendix A), confirming the reliability of our SED-fitting approach.

To explore the completeness of the sample we can take into account that when the AGN is not dominant in the MIR band, i.e. its contribution to the total emission is <50 per cent, our SED-fitting procedure might start failing in identifying the presence of an AGN. We therefore looked for all the sources identified as SFGs from our SED-fitting procedure (i.e. with no significant AGN component) with AGN luminosity upper limits above our IR quasar selection threshold of $\log\ \nu L_{6\,\mu m,\ AGN} \geq 44.78$ erg s^{-1}. There is only one SFG satisfying this condition, having $\log\ \nu L_{6\,\mu m,\ AGN} < 44.85$ erg s^{-1}. This source is classified as an AGN from its X-ray emission ($\log L_X \approx 43.2$ erg s^{-1}). Given its modest X-ray luminosity and since the $L_{6\,\mu m,\ AGN}$ upper limit is very close to our IR quasar luminosity threshold (only a factor of ∼1.2 higher), the AGN within this SFG might still not fulfil our selection criteria, i.e. its intrinsic power could be below our luminosity cut. For this reason we do not include this source in our sample, keeping in mind that our selection might not be 100 per cent complete in identifying IR quasars when the SF luminosity is very high.

We note, however, that our IR quasar selection through the SED analysis is more reliable than the typical MIR colour–colour

Table 1. IR quasar sample. (1) Source number; (2) MIR 3.6 μm source position, RA and Declination; (3) X-ray source identification number from Alexander et al. (2003) in CDF-N and from Xue et al. (2011) in CDF-S; the suffix 'N' and 'S' refer to North and South, respectively; (4) redshift; 's' and 'p' indicate the spectroscopic and photometric redshifts, respectively (Section 2.1); (5) logarithm of the X-ray luminosity at rest-frame 2–10 keV, extrapolated from the measured 0.5–2 keV flux (or upper limit), in units of erg s^{-1}; (6) logarithm of the rest-frame 6 μm luminosity of the AGN measured from the best-fitting SEDs in units of erg s^{-1}; (7) contribution from the AGN emission to the total (AGN + SF) emission at 6 μm; (8) logarithm of the AGN IR luminosity (8–1000 μm) in units of erg s^{-1}; (9) logarithm of the AGN bolometric luminosity, derived from L_{AGN}, in units of erg s^{-1}; (10) logarithm of the IR luminosity (8–1000 μm) of the star formation component in units of erg s^{-1}; (11) star formation rate in units of $M_{\odot}$ yr^{-1}; (12) logarithm of the rest-frame 2–10 keV luminosity produced by SF, estimated assuming the Lehmer et al. (2010) relation between SFR and hard X-ray luminosity; (13) estimated contribution from SF to the rest-frame 2–10 keV luminosity (uncorrected for absorption); (14) optical spectroscopic classification from Steidel et al. (2002), Barger et al. (2003) and Trouille et al. (2008) for the sources in GH-N and from Szokoly et al. (2004) and Silverman et al. (2010) in GH-S: broad-line AGN (BL), high-excitation emission line galaxies (HEG); star-forming galaxies (SF).

No (1)	Coordinates (2)	XID (3)	Redshift (4)	L_X (5)	$\nu L_{6\,\mu m,AGN}$ (6)	f_{AGN} (7)	L_{AGN} (8)	L_{bol} (9)	L_{SF} (10)	SFR (11)	$L_{X,SF}$ (12)	$f_{X,SF}$ (13)	Opt. class (14)
1	12:36:00.16 +62:10:47.4	–	2.002s	<42.30	45.44	80%	46.01	46.31	46.21	723	41.61	>20%	
2	12:36:22.94 +62:15:26.5	137N	2.583s	44.80	45.57	100%	46.09	46.39	<45.65	<197	<41.19	0%	BL
3	12:36:32.55 +62:07:59.8	171N	1.995s	42.69	45.33	94%	45.85	46.15	<45.22	<73	<40.87	<2%	HEG
4	12:36:35.60 +62:14:24.0	190N	2.005s	42.90	45.55	83%	46.13	46.43	46.29	858	41.66	6%	HEG
5	12:36:42.19 +62:17:11.2	223N	2.730s	43.93	44.81	76%	45.53	45.83	45.70	221	41.23	0%	
6	12:36:46.72 +62:14:45.9[a]	243N	2.004s	42.05	44.90	74%	45.44	45.74	45.84	306	41.33	19%	
7	12:36:49.65 +62:07:38.1	259N	1.610s	44.04	45.37	94%	45.92	46.22	45.51	145	41.09	0%	HEG
8	12:36:55.82 +62:12:01.2	287N	2.737s	43.06	44.96	69%	45.66	45.96	45.94	390	41.41	2%	
9	12:36:56.47 +62:19:37.6	–	1.80 p	<42.33	45.01	73%	45.54	45.84	45.95	396	41.41	>19%	
10	12:36:57.93 +62:21:28.7	299N	2.36 p	44.12	44.83	74%	45.16	45.46	45.88	332	41.36	0%	
11	12:36:59.32 +62:18:32.4	307N	2.14 p	42.74	44.96	83%	45.68	45.98	45.64	195	41.18	3%	
12	12:37:04.34 +62:14:46.2	–	2.214s	<42.09	45.11	91%	45.85	46.15	45.41	114	41.01	>4%	HEG
13	12:37:06.87 +62:17:02.1	344N	1.019s	44.14	44.79	90%	44.92	45.22	45.17	65	40.83	0%	BL
14	12:37:16.67 +62:17:33.3	390N	1.146s	43.70	44.95	98%	45.47	45.77	44.58	17	40.39	0%	SF
15	12:37:19.87 +62:09:55.2	398N	2.647s	43.77	44.92	85%	45.45	45.75	45.54	155	41.11	0%	SF
16	12:37:26.50 +62:20:26.6	423N	1.750s	42.74	45.42	89%	46.12	46.42	45.84	303	41.33	4%	
17	12:37:39.50 +62:15:58.6	–	2.98 p	<42.76	44.84	66%	45.57	45.87	45.97	414	41.43	>5%	
18	12:37:42.53 +62:18:11.8	459N	2.309s	44.70	44.98	93%	45.25	45.55	<45.30	<88	<40.93	0%	BL
19	12:37:57.28 +62:16:27.4	478N	2.922s	44.41	45.01	66%	45.48	45.78	46.01	458	41.46	0%	BL
20	03:32:09.45 −27:48:06.7	149S	2.810s	43.96	45.91	100%	46.22	46.52	<45.80	<280	<41.30	0%	BL
21	03:32:11.78 −27:46:28.2	176S	2.81 p	43.81	44.95	92%	45.12	45.42	<45.39	<109	<41.00	0%	
22	03:32:20.05 −27:44:47.2	278S	1.897s	42.43	44.85	73%	45.57	45.87	45.82	291	41.31	8%	HEG
23	03:32:23.44 −27:42:55.2	320S	2.145s	42.24	44.81	80%	45.50	45.80	45.59	174	41.15	8%	
24	03:32:23.72 −27:44:11.8	–	2.060s	<42.00	44.82	83%	45.38	45.68	45.34	97	40.96	>9%	
25	03:32:24.49 −27:50:45.8	–	2.630s	<42.06	44.90	88%	45.63	45.93	<45.39	<108	<40.99	9%	
26	03:32:25.14 −27:42:19.2	344S	1.617s	43.77	44.89	66%	45.44	45.74	46.00	438	41.44	0%	BL
27	03:32:25.69 −27:43:05.7	351S	2.291s	43.79	45.46	100%	45.74	46.04	<45.37	<103	<40.98	0%	HEG
28	03:32:28.82 −27:48:29.7	–	2.550s	<41.95	45.27	78%	45.97	46.27	45.93	375	41.39	>28%	
29	03:32:31.47 −27:46:23.2	435S	2.220s	42.44	45.01	75%	45.30	45.60	45.95	397	41.41	9%	HEG
30	03:32:35.72 −27:49:16.0	490S	2.579s	42.53	45.43	78%	46.08	46.38	46.29	866	41.66	14%	HEG
31	03:32:37.76 −27:52:12.2	518S	1.603s	44.17	45.32	94%	45.67	45.97	<45.61	<180	<41.16	0%	HEG
32	03:32:37.79 −27:42:32.8	–	2.975s	<42.57	45.35	96%	46.07	46.37	<45.78	<269	<41.29	5%	
33	03:32:49.58 −27:47:14.9	–	2.600s	<42.33	44.81	94%	45.54	45.84	<45.26	<81	<40.90	4%	

Notes: [a]For this source, we report the X-ray coordinates as the 3.6 μm coordinates are centred on a low-redshift galaxy ($z = 0.556$) lying ≈1.8 arcsec from the X-ray source. Careful inspection of the multiwavelength images has proved that although the *Spitzer*-IRAC bands are dominated by the low-z galaxy emission, the emission at $\lambda \geq 8$ μm is centred at the X-ray source position rather than the 3.6 μm position of the low-z galaxy. We therefore expect the contamination from the low-z galaxy to be very small at the wavelengths used in our SED analyses of this IR quasar (see Section 3.1).

selections used to identify AGN (e.g. Stern et al. 2005; Lacy et al. 2007; Donley et al. 2012), as the SED analysis accounts for the source redshifts and corrects for any contamination from SF to the MIR emission, contrary to any of the colour–colour selection techniques. Indeed, despite our sources being the most luminous quasars at MIR wavelengths within the GH fields, the Stern et al. (2005) AGN wedge would miss ≈20 per cent of them, as well as the majority of the less luminous AGN that we identified from the SED analysis (see Fig. 1), probably due to the contamination from SF and/or starlight to the emission in the MIR bands used in the colour–colour plot (typically *Spitzer*-IRAC bands). Also the Donley et al. (2012) AGN selection criteria would miss several of our IR quasars, selecting only ∼73 per cent of them. On the other hand, the Lacy et al. (2007) AGN wedge would select ∼97 per cent (all but one) of the IR quasars in our sample; however, a large fraction of the sources lying within the wedge are not identified as AGN according to our SED analysis, nor in the X-ray band, as SFGs at low and high redshifts can enter the Lacy et al. (2007) AGN locus, introducing significant contamination from non-AGN (e.g. Donley et al. 2012).

Of our final sample of 33 luminous IR quasars, 24 (∼73 per cent) are detected in the X-ray band (Section 2.2). The X-ray identification number of these sources (XID) and their rest-frame 2–10 keV luminosity (L_X) are reported in Table 1. These luminosities are extrapolated from the observed 0.5–2 keV fluxes reported in the Alexander et al. (2003) and Xue et al. (2011) catalogues for the

Table 2. X-ray spectral results for all of the X-ray-detected sources. (1) Source number as in Table 1; (2) XID as in Table 1; (3) net counts in the *Chandra* spectra in the observed 0.5–8 keV energy range; (4) photon index, which was left free to vary in our spectral fits (model 1); (5) intrinsic hydrogen column density in units of 10^{22} cm^{-2}; (6) photon index obtained from model 2; $\Gamma = 1.80$ has been fixed where the spectral fits could not reliably constrain the spectral slopes and $N_{\rm H}$ simultaneously (Section 4.1.1); (7) hydrogen column density obtained from model 2, in units of 10^{22} cm^{-2}; (8) fraction of the intrinsic power-law emission that is scattered at soft energies ($E < 2$ keV); (9) logarithm of the rest-frame 2–10 keV luminosity, in units of erg s^{-1}; (10) logarithm of the intrinsic, i.e. corrected for absorption, 2–10 keV luminosity (rest frame), in units of erg s^{-1}.

No (1)	XID (2)	Net counts (3)	$\Gamma_{\rm mo1}$ (4)	$N_{\rm H,mo1}$ (5)	$\Gamma_{\rm mo2}$ (6)	$N_{\rm H,mo2}$ (7)	$f_{\rm scatt}$ (per cent) (8)	log $L_{2-10\ \rm keV}$ (9)	log $L_{2-10\ \rm keV,intr}$ (10)
2	137N	3587	$1.77^{+0.05}_{-0.05}$	<0.8	–	–	–	44.72	44.72
3	171N	128	$0.28^{+0.74}_{-0.46}$	<15.3	1.80	$74.3^{+65.3}_{-32.8}$	7.4 ± 1.4	42.94	43.79
4	190N	159	$1.25^{+0.76}_{-0.74}$	$20.9^{+18.6}_{-15.4}$	$1.82^{+0.65}_{-0.67}$	$49.7^{+25.3}_{-21.5}$	7.9 ± 6.1	43.13	43.82
5	223N	421	$1.81^{+0.33}_{-0.30}$	$9.1^{+6.1}_{-5.0}$	$1.91^{+0.41}_{-0.34}$	$10.8^{+17.1}_{-4.6}$	7.4 ± 11.6	43.87	44.15
6	243N	12	$1.86^{+1.29}_{-0.87}$	–	1.80	<8.2	–	42.06	42.11
7	259N	2952	$1.86^{+0.13}_{-0.12}$	$8.2^{+1.2}_{-1.1}$	$1.93^{+0.14}_{-0.13}$	$10.6^{+1.9}_{-1.8}$	4.2 ± 1.3	44.22	44.49
8	287N	56	$1.91^{+0.41}_{-0.50}$	<2.6	–	–	–	43.00	43.00
10	299N	795	$1.66^{+0.21}_{-0.12}$	<1.5	–	–	–	44.05	44.05
11	307N	89	$1.29^{+0.83}_{-0.83}$	$13.8^{+17.6}_{-12.8}$	$1.71^{+1.39}_{-1.29}$	$39.2^{+54.4}_{-36.1}$	7.2 ± 6.5	42.92	43.54
13	344N	7007	$2.05^{+0.04}_{-0.04}$	<0.8	–	–	–	44.03	44.03
14	390N	2780	$1.48^{+0.10}_{-0.10}$	$1.5^{+0.4}_{-0.4}$	$1.65^{+0.15}_{-0.14}$	$3.9^{+1.7}_{-1.5}$	26.5 ± 6.5	43.89	44.00
15	398N	414	$1.76^{+0.35}_{-0.32}$	$14.5^{+7.7}_{-6.3}$	$1.95^{+0.59}_{-0.48}$	$29.9^{+28.9}_{-17.6}$	13.4 ± 10.9	43.75	44.12
16	423N	114	$0.54^{+0.56}_{-0.41}$	<5.6	1.80	$137.3^{+238.7}_{-105.1}$	10.9 ± 1.9	42.92	43.84
18	459N	3301	$1.76^{+0.08}_{-0.06}$	<0.4	–	–	–	44.62	44.62
19	478N	890	$2.05^{+0.20}_{-0.13}$	<1.6	–	–	–	44.35	44.35
20	149S	1286	$1.69^{+0.18}_{-0.18}$	$20.6^{+5.1}_{-4.9}$	–	–	–	43.91	44.37
21	176S	677	$1.93^{+0.27}_{-0.25}$	$13.2^{+6.0}_{-5.1}$	$2.40^{+0.52}_{-0.48}$	$41.8^{+23.9}_{-24.6}$	15.1 ± 7.9	43.70	44.07
22	278S	165	$1.35^{+1.01}_{-1.03}$	$68.7^{+44.9}_{-38.4}$	$1.75^{+1.07}_{-1.21}$	$89.8^{+47.4}_{-50.6}$	0.8 ± 0.5	42.89	44.01
23	320S	48	$-0.73^{+0.59}_{-0.97}$	–	1.80	$234.8^{+176.0}_{-104.2}$	1.5 ± 0.2	41.95	43.65
26	344S	1680	$2.10^{+0.16}_{-0.14}$	$0.7^{+0.6}_{-0.5}$	–	–	–	43.69	43.73
27	351S	1378	$1.70^{+0.18}_{-0.17}$	$13.7^{+3.1}_{-2.7}$	$1.76^{+0.24}_{-0.20}$	$16.4^{+7.6}_{-4.2}$	3.8 ± 4.9	43.82	44.15
29	435S	59	$1.11^{+0.46}_{-0.44}$	<0.8	$1.89^{+0.67}_{-0.61}$	$1100.2^{+1235.4}_{-695.8}$	2.8 ± 2.9	42.46	44.03
30	490S	82	$0.37^{+1.76}_{-0.76}$	<76.0	1.80	$2591.4^{+2037.2}_{-1464.5}$	0.5 ± 0.1	42.55	44.86
31	518S	4961	$2.17^{+0.08}_{-0.08}$	$2.1^{+0.4}_{-0.3}$	–	–	–	44.17	44.27

GH-N and GH-S sources, respectively, using a photon index $\Gamma = 1.8$ and appropriate *k*-correction. This simple extrapolation is performed to have a first idea of the discrepancy between the observed X-ray and the MIR emission of our quasars. We caution, however, that this X-ray luminosity calculation does not account for the possible contribution from SF to the observed X-ray flux (see Table 1 and Section 4.3). Accurate estimates of the observed and intrinsic 2–10 keV luminosity for the X-ray-detected sources, derived from spectral analyses, are obtained in Section 4.1 and reported in Table 2; we use these luminosities for further analyses throughout the paper.

4 ANALYSES AND RESULTS

In this section, we present the X-ray spectral analysis performed on all of the X-ray-detected IR quasars (24 sources) to constrain the absorbing column density ($N_{\rm H}$) and therefore derive the intrinsic X-ray luminosity. We then estimate the obscured quasar ($N_{\rm H}$>10^{22} cm^{-2}) and CT quasar ($N_{\rm H}$>1.5×10^{24} cm^{-2}) fractions from the X-ray spectral fitting results and from a comparison between the observed (i.e. not corrected for absorption) 2–10 keV luminosity and the $L_{6\,\mu\rm m,\ AGN}$ (rest-frame), used as a proxy of the intrinsic AGN power. We then investigate in detail the host galaxy properties through the SFRs estimated from the $L_{\rm SF}$ derived from the SED-fitting analysis, in relation to the AGN intrinsic luminosity and X-ray obscuration. We finally explore the impact of galaxy mergers/interactions in quasar hosts by visually classifying the host galaxy morphology disturbance of our IR quasars using high-resolution *HST* images.

4.1 X-ray spectroscopy

For all of the 24 IR quasars with an X-ray detection in the CDF-N and CDF-S catalogues (Alexander et al. 2003; Xue et al. 2011), we performed X-ray spectral analyses to investigate the high-energy properties of these sources. For the X-ray-undetected sources, we estimated 3σ flux upper limits through aperture photometry on the *Chandra* images, assuming a spectral slope of $\Gamma = 1.4$ for the count rate to flux conversion. The 2–10 keV luminosity upper limits derived from these fluxes are reported in Table 1.

The spectra were extracted using the AE software package (Broos et al. 2010, 2012) and grouped with a minimum of 20 counts per energy bin in order to adopt χ^2-fitting statistics. The spectra with limited counting statistics (<200 net counts at 0.5–8.0 keV) were binned with a minimum of one count per bin and the Cash statistic (Cash 1979) was adopted for the spectral analysis with XSPEC (v. 12.8.1g; Arnaud 1996).

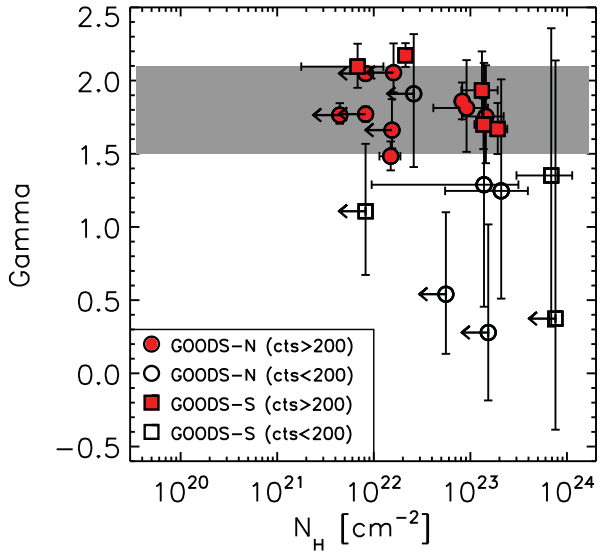

Figure 2. Photon index Γ versus intrinsic hydrogen column density (N_H) for the X-ray-detected IR quasars in our sample, obtained using a simple absorbed power-law model (model 1); the sources XID 243N and XID 320S are not included in the plot because the Γ and N_H parameters could not be simultaneously constrained from the spectral fit due to the low numbers of counts (<50 cts; see Section 4.1). Sources in GH-N and GH-S are represented by circles and squares, respectively. Red filled symbols indicate sources with more than 200 net counts in the $E = 0.5$–8 keV spectra; open symbols are sources with <200 net counts (i.e. with poor counting statistics). The grey shaded region represents the intrinsic photon indices typically found for AGN ($\Gamma = 1.8 \pm 0.3$; e.g. Nandra & Pounds 1994; Mainieri et al. 2002; Mateos et al. 2005; Tozzi et al. 2006). The quasars with low numbers of counts have typically flat photon indices ($\Gamma < 1.5$), suggesting the presence of additional spectral components, such as soft scattered emission and/or reflection (Section 4.1.1).

4.1.1 Basic spectral model fitting

We initially used a simple absorbed power-law model to characterize the source spectra (model 1), in addition to Galactic absorption, which was fixed to the average values of $N_{H,\,Gal} = 10^{20}$ cm^{-2} in GH-N and $N_{H,\,Gal} = 9.0 \times 10^{19}$ cm^{-2} in GH-S (Dickey & Lockman 1990). We left the photon index Γ and the intrinsic hydrogen column density (N_H) as free parameters. In Fig. 2, we show the Γ versus N_H obtained from these fits. For two quasars (XID 243N and XID 320S; see Table 1) with very low numbers of counts (<50 net counts, 0.5–8.0 keV), we only fit a simple power-law model with no intrinsic absorption as no useful constraints could be obtained simultaneously on Γ and N_H from model 1. These two sources are not plotted in Fig. 2. The results of the X-ray spectral analysis (including errors at 90 per cent confidence level) are reported in Table 2. We note that 14 of the 24 analysed sources (∼58 per cent) have good counting statistics (net counts >200; see Table 2). For these sources we obtained good spectral constraints with our simple model, with spectral slopes consistent with the intrinsic values typically found for AGN ($\Gamma = 1.8 \pm 0.3$; e.g. Nandra & Pounds 1994; Mainieri et al. 2002; Mateos et al. 2005; Tozzi et al. 2006). The sources with lower counting statistics (net counts <200) have typically flatter spectral indices, ranging between $\Gamma \approx 0.3$–1.4, with large errors. This indicates that the spectra of these sources are harder, and likely more obscured than those measured for the sources with higher numbers of counts; however the poor counting statistics do not allow us to simultaneously place tight constraints on the spectral parameters, Γ and N_H, as they are degenerate for low-count spectra (e.g. Mateos et al. 2008). The flat Γ in these sources might also indicate that a simple absorbed power-law model does not properly characterize their X-ray emission and additional spectral components might be required (e.g. soft scattered component, or reflection).

For the sources with a flat photon index ($\Gamma < 1.5$), we therefore included an extra power-law component in the model to fit the emission at soft energies ($E \lesssim 1$ keV; hereafter model 2). There are several processes that can cause emission at soft X-ray energies, such as thermal emission from star-forming regions, radio jets, atomic processes in partially ionized gas, partial covering by a neutral absorber, or blurred ionized reflection from the inner parts of the accretion disc (e.g. Turner et al. 1997; Gierliński & Done 2004); however, given the limited numbers of counts available in our spectra it is not possible to fit more complex models. We therefore assume a power-law model as an approximation of the soft X-ray emission, with the photon index Γ tied to that of the primary power law (e.g. Brightman et al. 2014; Buchner et al. 2014; Lanzuisi et al. 2015) to limit the number of free parameters in the model.[6] Fitting the spectra with model 2 constrained the power-law slopes to more typical values for AGN (see Table 2), although the uncertainties on the parameters are still large. Where reasonable constraints on Γ could not be obtained, we fixed $\Gamma = 1.8$ to obtain better constraints on the column densities. The N_H values resulting from the fitting of model 2 are typically higher than those obtained from model 1 and in some cases they are very high ($N_H > 8 \times 10^{23}$ cm^{-2}) and possibly consistent with CT absorption. In two cases (XID 435S and XID 490S; see Section 4.1.3), the column densities estimated by model 2 even exceed $N_H > 10^{25}$ cm^{-2}. Although these N_H values are not reliable because the simple parametrization of the spectra with an absorbed power law is not suitable to constrain column densities of $N_H >$ few $\times 10^{23}$cm^{-2}, they still indicate that these sources might indeed be heavily obscured, possibly CT. We investigate this hypothesis using more suitable models in Section 4.1.2. In model 2, we also estimated the fraction of intrinsic emission scattered at soft energies (f_{scatt}), calculated from the ratio between the normalizations of the scattered and intrinsic power-law components, which is on average only a few per cent, typically $\lesssim$5 per cent (e.g. Turner et al. 1997; Ueda et al. 2007). However, in some cases we find higher scattered fractions (see Table 2), which might be due to the contribution from SF emission to the soft energy spectrum ($E <$ 1–2 keV).

We also tested model 2 for sources showing significant X-ray absorption ($N_H > 10^{22}$ cm^{-2}) from the fitting of model 1, but with steeper spectral slopes ($\Gamma > 1.5$); the results are reported in Table 2 for all of the sources where the normalization of the soft scattered power law could be constrained. Although the column densities obtained from these fits are typically higher than those obtained from model 1, the scatter on the parameters (Γ and N_H) is larger and in all cases the results from the two models are consistent. We therefore use the best-fitting solutions from model 1 to estimate the luminosity for these sources.

From the best-fitting models (model 1 for the sources with $\Gamma_{mo1} > 1.5$, and model 2 for the remainders), we calculated the rest-frame 2–10 keV luminosity of the X-ray-detected IR quasars ($L_{2-10\,keV}$),

[6] We also tested the spectral fits of model 2 with a soft power-law slope free to vary, but no useful constraints could be obtained on Γ for our quasars, due to the limited counting statistics and the high redshift of the sources, which shifts most of the soft energy emission ($E \lesssim$ 1–2 keV, rest frame) out of the *Chandra* sensitivity range.

Table 3. Spectral fits of the heavily obscured quasars using PLCABS (Yaqoob 1997) and Torus (Brightman & Nandra 2011).

		PLCABS		Torus[a]	
No	XID	Γ^b	$N_H{}^c$	Γ^b	$N_H{}^c$
3	171N	1.8	$79.1^{+54.4}_{-39.4}$	1.8	>332.5
4	190N	$1.76^{+0.70}_{-0.72}$	$45.0^{+24.9}_{-21.1}$	$1.71^{+0.71}_{-0.71}$	$39.8^{+27.6}_{-18.1}$
11	307N	1.8	$43.8^{+75.9}_{-26.0}$	$2.39^{+0.48}_{-0.39}$	>603.8[d]
16	423N	1.8	$42.7^{+231.1}_{-28.0}$	1.8	$137.4^{+195.9}_{-125.6}$
20	149S[d]	$1.73^{+0.16}_{-0.16}$	$21.9^{+4.0}_{-3.9}$	$1.74^{+0.14}_{-0.17}$	$19.6^{+3.2}_{-3.9}$
22	278S	1.8	$84.3^{+18.8}_{-15.7}$	1.8	$78.1^{+18.4}_{-16.6}$
23	320S	1.8	$181.2^{+121.3}_{-67.2}$	1.8	$159.8^{+153.7}_{-54.2}$
29	435S	$1.90^{+0.70}_{-0.62}$	$685.4^{+885.0}_{-424.2}$	$1.90^{+0.84}_{-0.74}$	$251.4^{+368.6}_{-135.9}$
30	490S	1.8	$1013.4^{+1962.7}_{-819.9}$	1.8	>429.5

Notes: [a]To fit the Torus model, we fixed the opening angle to $\theta_{tor} = 60^\circ$ and the inclination angle to $\theta_{inc} = 80^\circ$, since these sources have typically poor counting statistics and these parameters cannot be constrained from the spectral fits. [b]Where sensible constraints could not be obtained simultaneously for the photon index Γ and the column density N_H, we fixed $\Gamma = 1.8$. [c]The column density N_H is expressed in units of 10^{22} cm^{-2}. [d]For this source, we did not include any soft power-law component as it is not needed in the fit.

as well as the unabsorbed 2–10 keV luminosity ($L_{2-10\,keV,intr}$), i.e. corrected for the best estimate of the N_H (Table 2).

4.1.2 *Spectral models for heavily obscured AGN*

From the spectral analysis using the simple models 1 and 2, for nine sources we obtained very large column density values (see Table 2) indicating that they are heavily obscured (defined here as: $N_H > 2 \times 10^{23}$ cm^{-2}), or CT sources ($N_H > 1.5 \times 10^{24}$ cm^{-2}). However, simple absorbed power-law models are not suitable to reliably constrain such large column densities, as they do not accurately account for the Compton scattering and reflection of the absorbed photons through an optically thick material. We therefore modelled the intrinsic emission of these sources using more appropriate models, such as: (i) PLCABS (Yaqoob 1997), which simulates the attenuation of a power-law continuum by dense, cold matter, and (ii) Torus (Brightman & Nandra 2011), which is a table model based on Monte Carlo simulations of X-ray radiative transfer, self-consistently taking into account Compton scattering and iron fluorescence emission. To represent the soft X-ray emission we used a power-law model, as in model 2. To fit the PLCABS model we left N_H and Γ free to vary, with Γ tied to that of the soft power-law component; where both parameters cannot be constrained due to low counting statistics, we fixed $\Gamma = 1.8$. The maximum number of scatters in the model was set to 12 (see Yaqoob 1997), and all other parameters were fixed to their default values. For the Torus model we fixed the inclination angle to an edge-on view, $\theta_{inc} = 80^\circ$, and an opening angle[7] of $\theta_{tor} = 60^\circ$ (see Brightman & Ueda 2012). The N_H and Γ parameters were left free to vary, with Γ tied to that of the soft scattered component, as for the PLCABS model, or fixed to $\Gamma = 1.8$. The best-fitting parameters obtained with these two models are reported in Table 3.

[7] We note that we also tried the fits with $\theta_{tor} = 30^\circ$, however, due to the limited numbers of counts in the spectra it was not possible to determine which of the two geometries provided the best fit.

In general, there is good agreement between the results obtained from the PLCABS and the Torus models. Although the parameters are not tightly constrained, as the errors are relatively large, all the model solutions resulting from our analyses indicate that these quasars are, in fact, heavily obscured and in some cases, as for XID 320S, XID 435S and XID 490S, even CT. We note that three more sources, XIDs 171N, 307N and 423N are consistent with being CT quasars within the uncertainties on the N_H parameter (Table 3).

4.1.3 *Notes on some individual sources*

Although most of the source spectra can be fitted with the simple models described in the previous sections, and sensible results are obtained for their spectral parameters (see Tables 2 and 3), some of the sources show some peculiar characteristics. Here, we describe in more detail the most interesting sources amongst our X-ray-detected IR quasar sample.

XID 171N. From the spectral fits using model 2 and PLCABS this $z = 1.995$ source shows a very high level of absorption $N_H \approx 8 \times 10^{23}$ cm^{-2} ($\Gamma = 1.8$), although not at CT levels. However, the residuals in the hard band ($E \gtrsim 3$ keV, observed frame) suggest the presence of a reflection component and an emission line at $E \approx 2$ keV (observed frame), typical of CT AGN spectra. Indeed, the spectral fit using the Torus model yields a column density lower limit which is well within the CT regime. Georgantopoulos et al. (2009) have also classified this source as a CT AGN. The strong emission line is consistent with the redshifted iron Kα line ($E = 6.4$ keV) with an equivalent width of EW $= 1.2^{+1.6}_{-1.1}$ keV; given the limited counting statistics of the spectrum the uncertainties on the line EW are large, but still consistent with CT absorption.

XID 243N. The spectrum of this $z = 2.004$ source has only 12 net counts (0.5–8 keV) therefore a more complex model than a simple power law cannot be fit to the data. The effective photon index measured from the spectrum is $\Gamma = 1.86^{+1.29}_{-0.87}$. Fitting the spectrum with an absorbed power law with $\Gamma = 1.8$ fixed to try to constrain the level of absorption results in an upper limit of $N_H < 8 \times 10^{22}$ cm^{-2}, which is consistent with the source being unabsorbed. However, the X-ray luminosity of XID 243N is very low compared to the 6 μm luminosity measured from its IR SED (see Table 1) and the typical $L_X - L_{6\,\mu m}$ relations (e.g. Lutz et al. 2004; Fiore et al. 2009; Mateos et al. 2015). The observed X-ray luminosity is consistent with a suppression of a factor of ∼300 with respect to the intrinsic luminosity measured in the MIR (see Table 4), and still more than a factor of ∼120 considering the intrinsic scatter of the $L_X - L_{6\,\mu m}$ relation (∼0.35 dex; e.g. Mateos et al. 2015). This suggests that XID 243N might be a heavily CT quasar (see Section 4.2 and Fig. 3) and that the X-ray emission seen by *Chandra* is only the soft scattered component (typically a few per cent of the intrinsic nuclear emission; e.g. Turner et al. 1997; Ueda et al. 2007; Young et al. 2007, and references therein), or some emission due to SF in the host galaxy (see Table 1 and Section 4.3). Another possibility is that this source is intrinsically X-ray weak, as it has been found, for instance, for broad absorption line (BAL) quasars (see e.g. Luo et al. 2014). However, XID 243N has never been identified as a BAL quasar to date. Although the hypothesis of intrinsically weak X-ray emission cannot be ruled out for this quasar, we favour here the heavy-obscuration interpretation (see Section 4.2).

XID 287N. Similar to XID 243N, this $z = 2.737$ quasar has an apparently unobscured spectrum (with low numbers of counts) and an X-ray luminosity that is significantly smaller compared to the intrinsic AGN luminosity measured in the MIR band. Assuming a

Table 4. Indication of CT quasar classification from various diagnostics for our CT quasars candidates. (1) Source number as in Table 1; (2) XID as in Table 1; (3) CT quasar classification: sources that we consider as secure CT quasars, based on various diagnostics explored in our analyses are marked as 'CT'; all other sources are still CT quasar candidates; (4) X-ray spectral models yielding $N_{\rm H}$ values consistent, within the errors, with CT absorption $N_{\rm H}>1.5 \times 10^{24}$ cm^{-2}: 'M2' refers to model 2, 'P' to the PLCABS model and 'T' to the Torus model (see Sections. 4.1.1 and 4.1.2); (5) sources showing an iron Kα line emission with EW $\gtrsim$ 1 keV; (6) factor of suppression of the observed X-ray luminosity $L_{2-10{\rm keV}}$ compared to the intrinsic X-ray luminosity derived from the 6 μm luminosity ($L_{\rm X|6\,\mu m}$) using the Lutz et al. (2004) relation; the values in parentheses correspond to the suppression factors estimated using the lower boundary of the intrinsic $L_{\rm X}-L_{6\,\mu m}$ relation assuming a scatter of ∼0.35 dex; (7) logarithm of the intrinsic X-ray luminosity derived from optical emission lines, in units of erg s^{-1}; we adopted the average emission-line flux ratios from Netzer et al. (2006) and the [O III]$_{\lambda5007}$-X-ray flux ratio from Mulchaey et al. (1994); (8) list of emission lines detected in the optical spectra used to infer the intrinsic X-ray luminosity in column (7); (9) reference of previous work where these sources are classified as CT quasars, or CT quasar candidates: 1 = Alexander et al. (2008), 2 = Georgantopoulos et al. (2009), 3 = Georgantopoulos et al. (2011b), 4 = Georgantopoulos et al. (2011a); 5 = Brightman et al. (2014), 6 = Brightman & Ueda (2012) and 7 = Feruglio et al. (2011).

No (1)	XID (2)	Class (3)	$N_{\rm H}$ (4)	EW$_{\rm FeK\alpha}$ (5)	$L_{\rm X|6\,\mu m}/L_{2-10{\rm keV}}$ (6)	$L_{\rm X|lines}$ (7)	Notes (8)	Refs. (9)
1	–		–	–	>522 (>233)			1[e]
3	171N	CT	T	√	96 (43)			2
6	243N	CT	×	×	270 (120)	45.7	Lyα[a]	3
9	–		–	–	>289 (>129)			[e]
11	307N	CT	T	√	42 (19)			[e]
12	–	CT	–	–	>195 (>87)	44.4	Lyα, C IV, He II, C III][b]	1
16	423N	CT	M2, P, T	×	122 (54)			4[e]
17	–		–	–	>47 (>21)			[e]
23	320S	CT	M2, P, T	×	282 (126)			5[f]
24	–		–	–	>256 (>114)			
25	–		–	–	>273 (>122)			
28	–		–	–	>820 (>366)			[e]
29	435S	CT	M2, P, T	×	138 (62)		He II, C III][c]	6
30	490S	CT	M2, P, T	√	293 (131)	44.5	Lyα, C IV, He II, C III], Ne V[d]	6, 7[e]
32	–		–	–	>233 (>104)			
33	–		–	–	>119 (>53)			[e]

Notes: [a]Optical emission line information from Adams et al. (2011); [b]Alexander et al. (2008); [c]Daddi et al. (2004); [d]Szokoly et al. (2004) and Feruglio et al. (2011). [e]These sources also have MIR-to-optical colours typical of dust obscured galaxies (DOGs; see Fig. 7 and Section 5.2). [f]This source is border-line CT in Brightman et al. (2014), but consistent with CT absorption within the errors, with $N_{\rm H}$= (0.5–2.9) $\times 10^{24}$cm^{-2}.

standard value for $L_{\rm X}/L_{6\,\mu m}$ (e.g. Lutz et al. 2004; Fiore et al. 2009; Mateos et al. 2015), we estimate that the observed X-ray luminosity is consistent with being suppressed by a factor of ∼35 (see Table 4). This suppression is consistent with the effect of CT absorption, but it is less extreme than that observed for XID 243N. Moreover, no other diagnostics have been found to confirm the intrinsic AGN luminosity measured in the MIR band, therefore the possibility of intrinsic X-ray weakness cannot be ruled out.

XID 307N. In the lightly binned spectrum (1 count/bin) of this quasar, clear residuals around the observed ∼2 keV indicate the presence of a strong iron emission line, consistent with being Fe Kα at the source redshift of $z = 2.14$. We therefore added a Gaussian component to the fit, with $E = 6.4$ keV and line width fixed at $\sigma = 50$ eV, to measure the strength of the line. Since the redshift of this source is photometric, we initially left the redshift parameter in the model free to vary. From the X-ray spectral fit we obtained constraints on the redshift of $z = 2.18^{+0.08}_{-0.08}$, in good agreement with the photometric estimate reported in Table 1. Fixing $z = 2.18$ and fitting the spectrum, however, produces a very flat photon index of $\Gamma = 0.70^{+0.95}_{-0.62}$, and no constraints are found on the $N_{\rm H}$ parameter. Fixing $\Gamma = 1.8$ yields a column density of $N_{\rm H}$= $(4.8^{+8.2}_{-3.0}) \times 10^{23}$cm^{-2} with some residuals in the hard band ($E \gtrsim 2$ keV), suggesting a possible contribution from a reflection component in the spectrum. This hypothesis is supported by the high EW measured for the iron line, EW = $1.2^{+1.0}_{-0.8}$ keV (rest frame), which is typical of CT AGN. Indeed, fitting the spectrum with the Torus model results in a column density lower limit of $N_{\rm H} > 6 \times 10^{24}$ cm^{-2} (see Table 3), i.e. in the CT regime. We tested this result also fitting the source spectrum with a pure reflection dominated model (i.e. PEXRAV model; Magdziarz & Zdziarski 1995) with the reflection parameter $R = -1$ fixed, plus a Gaussian line, implying column density in excess of $N_{\rm H} > 10^{25}$ cm^{-2}. This model provides a similarly good fit to the data as the previous models, yielding a spectral index of $\Gamma = 2.07^{+0.37}_{-0.43}$. If XID 307N is really CT, its intrinsic luminosity would therefore be $L_{2-10\,{\rm keV,intr}} \approx 10^{45}$ erg s^{-1}.

XID 390N. This $z = 1.146$ quasar has a relatively strong iron Kα line (EW = $0.38^{+0.13}_{-0.14}$ keV, rest frame, $\sigma = 50$ eV fixed), which could be broad, as leaving σ free to vary in the fit, we obtain $\sigma <$ 556 eV. Clear residuals suggest the presence of another emission line at $E \approx 5.9$ keV (rest frame) with EW ≈ 0.28 keV, which could be a relativistically redshifted iron line from the inner parts of the SMBH accretion disc or an outflow (e.g. Fabian et al. 2000). Although very interesting, more investigation on the emission lines of this quasar is beyond the scopes of this paper.

XID 149S. This $z = 2.810$ quasar has a column density $N_{\rm H} \approx 2 \times 10^{23}$ cm^{-2} and a photon index $\Gamma \approx 1.7$ with all the models used to fit the spectrum (i.e. model 1, PLCABS and Torus); none of the models required the addition of a soft scattered power law.

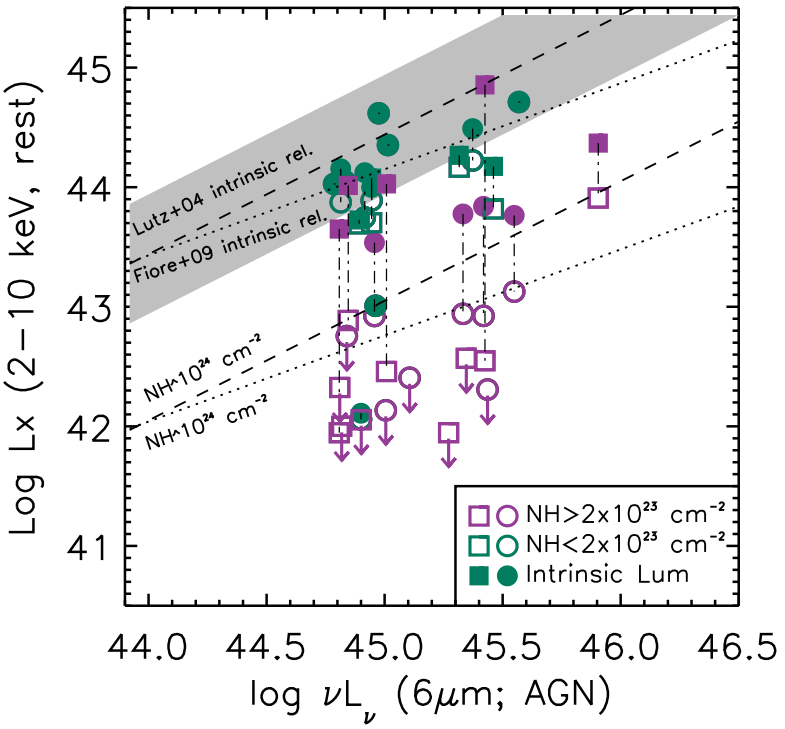

Figure 3. X-ray luminosity (2–10 keV rest frame) versus AGN rest-frame 6 μm luminosity (in units of erg s^{-1}) calculated from the SEDs; the observed X-ray luminosity (not corrected for absorption) is plotted with open symbols, while the intrinsic luminosity, i.e. corrected for the $N_{\rm H}$ measured from the X-ray spectra (reported in Table 2), is plotted with filled symbols. Unobscured and moderately obscured quasars ($N_{\rm H} < 2 \times 10^{23}$ cm^{-2}) are plotted in green, while the heavily obscured sources ($N_{\rm H} \geq 2 \times 10^{23}$ cm^{-2}) are plotted in magenta. Circles and squares correspond to sources in GH-N and GH-S, respectively. The shaded region represents the scatter of the intrinsic $L_{\rm X}-L_6$ μm relation from Lutz et al. (2004) (dashed line); the dotted line represents the Fiore et al. (2009) relation.

Although the X-ray spectrum does not show signs of any emission line, clear residuals around $E \approx 1.5$–2 keV ($E \approx 5.7$–7.6 keV, rest frame) indicate the presence of a strong absorption feature forming a P-Cygni type profile, which indicates the presence of a high-velocity outflow (e.g. Pounds & Reeves 2009; Tombesi et al. 2010). Indeed, this source has been identified in the optical band as a BAL quasar (Szokoly et al. 2004). A BAL quasar interpretation would help explaining why the intrinsic X-ray luminosity of this quasar, $L_{2-10\,{\rm keV,intr}} \approx 2 \times 10^{44}$ erg s^{-1}, which is corrected for the X-ray absorption derived from the spectral fitting, is lower than that expected from the MIR luminosity $\nu L_{6\,\mu{\rm m}} \approx 8 \times 10^{45}$ erg s^{-1}(see Fig. 3), as BAL quasars have been found to be intrinsically X-ray weak (e.g. Luo et al. 2014).[8]

XID 435S. Fitting this source spectrum with model 2 (see Section 4.1) results in a column density of $N_{\rm H} = (1.1^{+1.2}_{-0.7}) \times 10^{25}$cm^{-2} (with $\Gamma = 1.89^{+0.7}_{-0.6}$), which is consistent with heavily CT material. Using the PLCABS and Torus models, we obtained smaller $N_{\rm H}$ values of $N_{\rm H} \approx (3–7) \times 10^{24}$ cm^{-2} ($\Gamma \approx 1.9$), but still consistent with the source being CT (Table 3). However the spectrum does not show a clear signature of a strong Fe Kα line. We note that, although these models are too complex for the limited counting statistics to provide tight constraints on the spectral parameters, the intrinsic 2–10 keV X-ray luminosity corrected for the CT column densities derived from the spectral fits is in good agreement with the expectations from the MIR 6 μm AGN luminosity, according to the $L_{\rm X}-L_{6\,\mu{\rm m}}$ relation. XID 435S was also classified as a CT AGN also by Brightman & Ueda (2012).

XID 490S. This $z = 2.579$ quasar shows evidence for a strong emission line, consistent with the redshifted Fe Kα line at $E = 6.4$ keV, with an equivalent width of EW > 1 keV (although the limited counting statistics prevent us from obtaining better constraints on the EW). The spectral-fitting results from model 2 constrained the intrinsic column density largely in the CT regime (see Table 1). As in the previous case, fitting the spectrum with PLCABS or Torus models constrains the column density to lower values than that obtained from model 2 ($N_{\rm H} \approx (4–10) \times 10^{24}$ cm^{-2}), but still consistent with heavily CT columns. Similar results were obtained by Feruglio et al. (2011) and Brightman & Ueda (2012), who identified this source as CT. As for XID 435S, the intrinsic X-ray luminosity estimated by correcting for the high $N_{\rm H}$ obtained from the spectral fit would place this source on the $L_{\rm X}-L_{6\,\mu{\rm m}}$ relation (see Fig. 3).

4.2 Obscured AGN fraction

From the X-ray spectral analysis of the X-ray-detected sources, we found that a large fraction of the IR quasars (≈67 per cent, 16 out of 24 sources) are absorbed in the X-ray band by column densities $N_{\rm H} > 10^{22}$ cm^{-2}. Of these sources, nine can be classified as heavily obscured (reported in Table 3), with $N_{\rm H} \geq 2 \times 10^{23}$ cm^{-2}, of which three (XIDs 320S, 435S and 490S) have CT column densities, in excess of $N_{\rm H} = 1.5 \times 10^{24}$ cm^{-2} in all the models we used (see Section 4.1); three more sources (XIDs 171N, 307N and 423N)

[8] The X-ray weakness of BAL quasars is typically estimated with respect to the optical band ($\alpha_{\rm OX}$; e.g. Luo et al. 2014). However, since BAL quasars have SEDs consistent with those of typical quasars in the optical-to-IR bands (e.g. Gallagher et al. 2007), we expect to see X-ray weakness relative to the MIR emission too.

are consistent with being CT based on their $N_{\rm H}$, depending on the adopted model (see Tables 3 and 4), and on the detection of a strong iron Kα emission line (EW $\gtrsim$ 1 keV) in the case of XID 171N and 307N. We therefore classify these six sources as CT quasars. Due to the limited numbers of counts in the spectra, however, the strong Fe Kα line expected in CT spectra cannot be detected for all of these CT quasars.

To assess whether our IR quasars are indeed heavily obscured, or CT, we compared the X-ray luminosity (2–10 keV, rest frame) with the AGN 6 μm luminosity measured from the best-fitting SEDs (see Section 3.1). Since the MIR band tends to be much less affected by obscuration than the X-ray band, the MIR luminosity is often used as a proxy for the intrinsic AGN luminosity (e.g. Lutz et al. 2004; Alexander et al. 2008; Gandhi et al. 2009; DM13). Indeed, while unobscured sources are expected to lie on the intrinsic $L_{\rm X}-L_{6\,\mu{\rm m}}$ relation (e.g. Lutz et al. 2004; Fiore et al. 2009; Gandhi et al. 2009; Mateos et al. 2015; Stern 2015), heavily obscured and CT sources, where the X-ray luminosity is strongly suppressed, are expected to have weak observed X-ray emission compared to the MIR emission, and therefore lie well below the $L_{\rm X}-L_{6\,\mu{\rm m}}$ relation. In Fig. 3, we show the rest frame $L_{2\text{-}10\,{\rm keV}}$ versus $L_{6\,\mu{\rm m,AGN}}$ for our IR quasars; open symbols represent the observed X-ray luminosity, while the filled symbols represent the intrinsic X-ray luminosity $L_{2-10\,{\rm keV,intr}}$, i.e. corrected for the $N_{\rm H}$ derived from the X-ray spectral fitting (see Table 2). The unobscured and moderately obscured sources (shown in green) tend to agree with the local intrinsic $L_{\rm X}-L_{6\,\mu{\rm m}}$ relation, although possibly showing a flatter slope than that defined by Lutz et al. (2004), more in agreement with Fiore et al. (2009). All of the heavily obscured IR quasars lie well below the correlation, in the region of the plot expected for CT AGN. Correcting their observed X-ray luminosity for absorption brings these sources much closer to the intrinsic $L_{\rm X}-L_{6\,\mu{\rm m}}$ relation, although they still lie systematically below. It is important to note that the $N_{\rm H}$ of heavily obscured sources, obtained from spectral analyses of $E < 10$ keV data alone and with the simple parametrization used here (i.e. models 1 and 2), could be underestimated, as shown in several X-ray studies of heavily obscured AGN performed using *Chandra* or *XMM–Newton* data together with hard X-ray data ($E > 10$ keV) from *NuSTAR* (e.g. Del Moro et al. 2014; Gandhi et al. 2014; Lansbury et al. 2014, 2015). For the three sources securely identified as CT quasars (XIDs 320S, 435S and 490S), the intrinsic X-ray luminosity results in very good agreement with that expected from the MIR luminosity; this is also true for XID 171N and 307N if we correct the X-ray luminosity for the $N_{\rm H}$ derived from the Torus model, which gives $\log L_{2-10\ {\rm keV,intr}} \approx 45.4$ erg s^{-1} and $\log L_{2-10\ {\rm keV,intr}} \approx 45.1$ erg s^{-1}, respectively, and possibly for XID 423N considering the large scatter on the $N_{\rm H}$ value. This gives an extra indication that these sources are indeed CT.

We also note that all of the X-ray-undetected IR quasars (nine sources), for which we plot the X-ray luminosity upper limits, lie in the region of the $L_{\rm X}-L_{6\,\mu{\rm m}}$ plane expected for CT sources, and therefore can be considered as CT candidates. Two of the X-ray-undetected quasars, #1 and #12, have been already investigated by Alexander et al. (2008) and were identified as CT on the basis of X-ray analyses and $L_{\rm X}-L_{6\,\mu{\rm m}}$ analyses. For #12, the intrinsic X-ray luminosity has also been estimated from the optical emission lines (see Alexander et al. 2008) using the average line ratio from Netzer et al. (2006) and the relation between the [O III]$_{\lambda5007}$ and X-ray fluxes from Mulchaey et al. (1994), yielding $\log L_{\rm X|lines} \approx 44.4$ erg s^{-1} (Table 4), in agreement with that estimated from the MIR emission. This suggests that this source is intrinsically luminous, further confirming the CT nature of this quasar. The evidence found for #12 also support our assumption that the X-ray-undetected IR quasars are CT candidates. We therefore infer that the fraction of X-ray obscured sources ($N_{\rm H} > 10^{22}$ cm^{-2}) in our sample is ≈76 per cent (25/33 quasars, including the X-ray-undetected quasars), with ≈55 per cent being heavily obscured quasars (18/33 with $N_{\rm H} > 2 \times 10^{23}$ cm^{-2}) and 15 out of 33 quasars (≈45 per cent) are likely to be CT.

From the $L_{\rm X}-L_{6\,\mu{\rm m}}$ comparison it also emerged that two sources having unabsorbed X-ray spectra (XID 243N and XID 287N; see Table 2) have much weaker X-ray luminosity than that expected from their MIR luminosity, although for XID 287N the $L_{\rm X}/L_{6\,\mu{\rm m}}$ ratio is not as extreme as for XID 243N (see Fig. 3). XID 243N was classified as a candidate CT AGN also by Georgantopoulos et al. (2011b) on the basis of its $L_{\rm X}/L_{6\,\mu{\rm m}}$ ratio, similarly to our analysis. The detection of a strong Ly α emission line in the optical spectrum, which was attributed to AGN emission rather than SF by Adams et al. (2011), allowed us to estimate the expected intrinsic X-ray luminosity (as for source #12) $\log L_{\rm X|lines} \approx 45.7$ erg s^{-1}, calculated assuming the average AGN Ly α to [O III]$_{\lambda5007}$ line ratio from Netzer et al. (2006) and the [O III]$_{\lambda5007}$ to X-ray flux ratio from Mulchaey et al. (1994). Although this luminosity is higher than that inferred from the MIR emission, possibly due to the uncertainties on the optical emission line ratios and perhaps to some contamination from SF emission to the Ly α flux, it supports the idea of XID 243N being intrinsically X-ray luminous; we therefore consider this source as CT (Table 4). In this case, if we assume that the observed $E < 8$ keV spectrum is only due to scattering (∼1–3 per cent) of the intrinsic heavily obscured emission, we estimate the intrinsic X-ray luminosity to be $\log L_{\rm X} \approx 43.6$ erg s^{-1}. This is in good agreement with the intrinsic $L_{\rm X}-L_{6\,\mu{\rm m}}$ relation, supporting our classification of this quasar as CT. For XID 287N no other diagnostic has been found to establish whether this source is intrinsically X-ray luminous (and therefore likely CT) or X-ray weak (e.g. Luo et al. 2014); we thus do not include this source amongst our CT quasar candidates.

In Table 4, we list all the CT quasars and CT quasar candidates identified in our analyses and the various indicators that point to a CT quasar classification, i.e. primarily the high column density ($N_{\rm H} > 1.5 \times 10^{24}$ cm^{-2}) and/or strong iron line (EW $\gtrsim$ 1 keV) derived from the X-ray spectral analysis, the suppression of the observed X-ray luminosity (more than a factor of ∼30 for CT sources) compared to the intrinsic X-ray luminosity expected from the 6 μm emission ($L_{\rm X|6\,\mu m}$), and other indicators found in the literature, such as the X-ray weakness compared to the intrinsic quasar luminosity derived from optical emission lines. The total fraction of CT quasars (and CT quasar candidates) in our sample is therefore ≈24–48 per cent (8–16 out of 33 quasars) and the total obscured quasar fraction is ≈79 per cent.

4.3 Star formation rates

Using the results from our SED-fitting analyses (Section 3.1) and the X-ray spectral analyses, we explore here the connection between the quasar properties, such as their luminosity and X-ray obscuration, and the host galaxy properties, defined in terms of the SFR. From the IR luminosity (8–1000 μm) of the SFG component, derived from the SED fitting (see Section 3.1), we calculated the SFR of the galaxies hosting our IR quasars. We assumed a Salpeter (1955) initial mass function and used the relation from Kennicutt (1998). The range of SFRs estimated for our sources is large, SFR≈17–866 M$_{\odot}$yr^{-1} (see Table 1). In Fig. 4, we show the SFR versus the X-ray column density $N_{\rm H}$ (left) and the AGN 6 μm luminosity (right) for

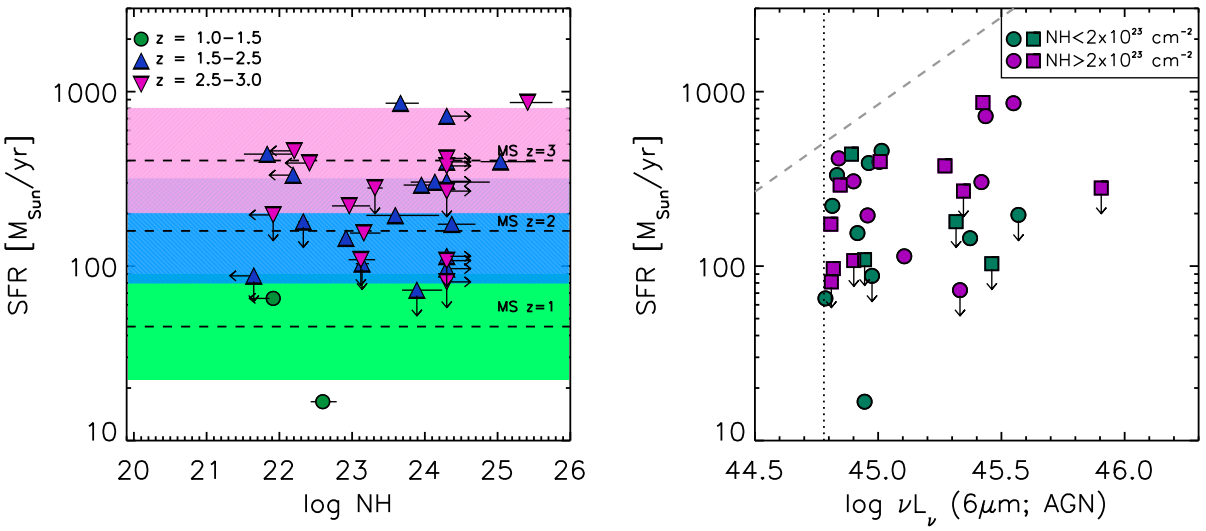

Figure 4. Left: SFR versus X-ray column density ($N_{\rm H}$) for the IR quasars (derived from the best fitting of model 1 or model 2); for the X-ray-undetected sources, which are CT quasar candidates, we fixed $N_{\rm H}$ at a lower limit of log $N_{\rm H}$>24.3 cm^{-2}. The sources have been divided in three redshift bins: $1.0 < z < 1.5$ (green circles), $1.5 < z < 2.5$ (blue triangles) and $2.5 < z < 3.0$ (magenta upside-down triangles). The dashed lines represent the main sequence (MS) SFRs at redshift $z = 1$, 2 and 3 (from bottom to top) for a stellar mass of $M_* = 9 \times 10^{10}$ M$_\odot$ (Elbaz et al. 2011), which is the average stellar mass found for X-ray-selected AGN at $z \approx 2$ by Mullaney et al. (2012); the shaded areas correspond to a factor of 2 above and below the MS at each redshift ($z = 1$: green, $z = 2$: blue and $z = 3$: pink). Right: SFR versus AGN 6 μm luminosity. Symbols are the same as in Fig. 3. The grey dashed line indicates the limit where the AGN contributes 50 per cent to the total luminosity at 6 μm; our IR AGN identification approach will be incomplete for SFRs above this dashed line. The vertical dotted line at log $\nu L_{6\,\mu\rm m} = 44.78$ erg s^{-1} marks our IR quasar selection.

the IR quasars in our sample, separating the heavily obscured from the unobscured/moderately obscured quasars (magenta and green symbols, respectively; see Section 4.2). In Fig. 4 (left), we divide our sample in three redshift bins: $z = 1.0$–1.5, 1.5–2.5 and 2.5–3.0 (green circles, blue triangles and magenta upside-down triangles, respectively), and compare their SFRs with those of typical main sequence (MS) SFGs at redshift $z \approx 1$–3 (e.g. Elbaz et al. 2011; Mullaney et al. 2012). In the figure, we plot the X-ray-undetected sources, which are CT quasar candidates, with a column density lower limit fixed to log $N_{\rm H}$>24.3 cm^{-2}. On average there is good agreement with the SFRs of our IR quasars and the MS in each redshift bin, however, at $z = 1.5$–2.5 there is a significant fraction of sources with SFRs more than a factor of 2 above the MS (6/18 sources in this redshift bin, i.e. ≈33 per cent), which could be classified as starburst galaxies; these sources also tend to have higher X-ray absorption ($N_{\rm H} > 2 \times 10^{23}$ cm^{-2}). On the other hand at $z = 2.5$–3.0 only one (heavily obscured) quasar out of 13 has SFR typical of starburst galaxies at similar redshift, while a significant fraction of our IR quasars (5/13 sources, ≈38 per cent) have SFRs below the MS. This possibly suggests a bias in our sample, as we are likely to miss quasars with very high SFRs (see also Fig. 4, right, and Section 3.2). We caution, however, that given the small number of sources in each redshift bin, these results are only tentative.

Overall, we do not find any significant correlation with the intrinsic AGN luminosity, $L_{6\,\mu\rm m,AGN}$, although the range in luminosity for our IR quasars is relatively narrow; this is in agreement with other studies by Harrison et al. (2012) and Stanley et al. (2015). Interestingly, on average we find that the most obscured quasars have higher SFRs than the unobscured quasars (see also Chen et al. 2015). However, as the number of sources in our sample is small, this difference is mainly driven by three heavily obscured sources with very high SFRs (≈700–900 M$_\odot$yr^{-1}, ∼16 per cent of the heavily obscured quasars) that are not representative of the average IR quasar host population, for which there seems to be no significant relation between SFR and X-ray obscuration (e.g. Lutz et al. 2010; Rosario et al. 2012; Rovilos et al. 2012).

From the measured SFRs, we calculate the expected X-ray emission at 2–10 keV (rest frame; $L_{\rm X,SF}$) produced by SF using the Lehmer et al. (2010) relation between SFR and rest-frame 2–10 keV luminosity (equation 4 in their table 4). The values are reported in Table 1. We also estimate what fraction of the observed X-ray luminosity (at 2–10 keV, rest frame) could therefore be due to SF (see Table 1). For the majority of the sources (≈82 per cent) the contribution from SF is negligible, of the order of <10 per cent. However, for ≈18 per cent of the sources more than 10 per cent of the observed X-ray luminosity could be due to SF and for some of them (#1, 6, 9 and 28) this contribution can reach up to ≈20–30 per cent. All of these quasars are candidates CT according to our analyses, of which 3 out of 4 are X-ray undetected. The relatively high contribution from SF to the 2–10 keV luminosity (or upper limit) supports the idea that in these quasars we do not detect the intrinsic AGN emission at X-ray energies, which is likely to be very heavily absorbed, as discussed in Section 4.1.3 for XID 243N (#6).

4.4 Host galaxy interactions

In order to test the major merger evolutionary scenario for quasars, which predicts that most of the accretion on to the SMBH happens in heavily obscured environments, due to large amounts of gas and dust driven to the centre of galaxies during the merger (e.g. Sanders et al. 1988; Di Matteo, Springel & Hernquist 2005; Hopkins et al. 2006, see also Alexander & Hickox 2012 for a review), we investigate here the connection between the X-ray obscuration and the host galaxy morphology of our IR quasars. In particular, we aim to explore whether the most obscured IR quasars are typically found in interacting/merging systems.

We used the high-resolution *HST* images to classify the galaxies in terms of disturbance or distortion of their morphology. The

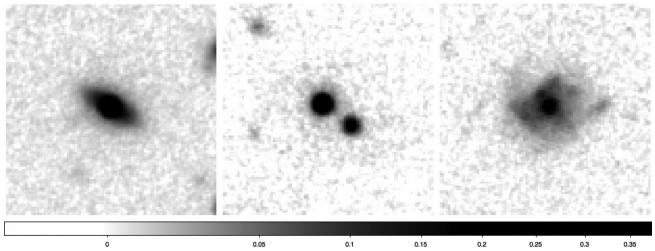

Figure 5. *HST F160W* (*H* band) image cutouts (6 arcsec × 6 arcsec) for three of our IR quasars showing examples of an 'undisturbed' galaxy (#14, left), a 'companion' class (#5, centre) and a 'disturbed' galaxy (#24, right). The source numbers are those reported in column (1) in Table 1.

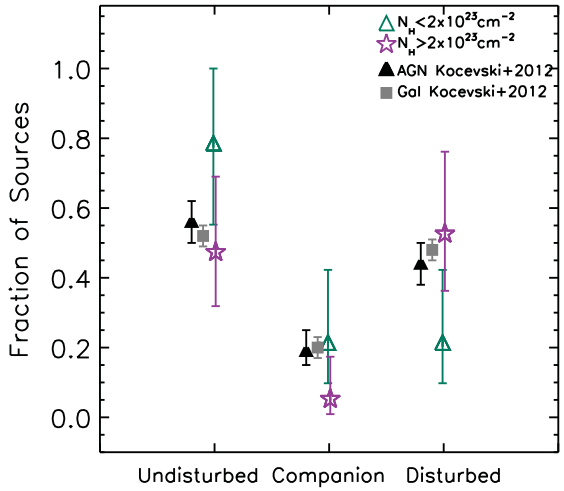

Figure 6. Fraction of IR quasar hosts with various disturbance classes, classified using *HST* images as described in Section 4.4. The fractions and 1σ uncertainties for the unobscured/moderately obscured quasar hosts ($N_{\rm H}<2 \times 10^{23}$ cm^{-2}) are plotted as green triangles and for the heavily obscured quasars ($N_{\rm H}\geq2 \times 10^{23}$ cm^{-2}) as magenta stars (see Section 4.2). The classes are divided into: 'undisturbed', 'companion' (which is a sub-class of the undisturbed galaxies) and 'disturbed'. For comparison the fractions for $z \approx 2$ AGN and non-AGN samples from Kocevski et al. (2012) are also shown (filled black triangles and grey squares, respectively). The disturbance fractions for our IR quasars are in good agreement with Kocevski et al. (2012). The unobscured/moderately obscured quasars reside preferentially in undisturbed systems, while the heavily obscured quasars are equally found in disturbed and undisturbed systems.

sources were visually classified mainly using the *H*-band images, however the supplementary information from the *V*, *z*, and *J* bands were also used (see Section 2.3). Following the visual classification method described in section 4 of Kocevski et al. (2012), the galaxies were initially classified as: (1) 'mergers', where strong signatures of distortions and/or multiple nuclei in a single coalescing system were visible; (2) 'interactions', i.e. systems with two distinct galaxies clearly showing interaction features, like tidal streams; (3) 'distorted', individual galaxies with no visible companion, but showing asymmetric morphology or distortions; (4) 'double nuclei', i.e. galaxies with multiple nuclei in a single coalesced system; (5) 'close pairs', where two (or more) galaxies lie within ∼1.5–2.0 arcsec (corresponding to ∼13–17 kpc at $z \approx 2$), although no signs of interactions are visible (which could mean the pairs are just line-of-sight alignments); (6) 'not-disturbed', single galaxies with no distortion/interaction signatures. We adopted the same classification method as in Kocevski et al. (2012) in order to allow direct comparison between our results and those presented for their galaxy and AGN samples, which we consider here as control samples for our IR quasars (as they span similar *z* ranges).

Since the number of sources in our sample, and therefore in each class of objects, is small, we grouped the disturbance classes listed above in two main groups, following Kocevski et al. (2012): (a) *'Disturbed'*, which include all galaxies showing any indication of distortion or interaction, i.e. classes (1), (2) (3) and (4); this group corresponds to the *Disturbed II* class in Kocevski et al. (2012); (b) *'Undisturbed'*, i.e. all sources in classes (5) and (6). Although class (5), hereafter defined as *'Companion'* group, is a sub-class of the undisturbed group, we also consider it separately, as despite the fact that these close pairs do not show visible signs of distortions/interactions they might still be associated. Examples of these three groups are shown in Fig. 5. To test the robustness of our classification method, we compare our disturbance classification for the IR quasars in the GH-S field with the visual classification performed by the CANDELS team (e.g. Kartaltepe et al. 2012), described in section 2.1.2 of Rosario et al. (2015).[9] For details on the classification method and the reliability of the classification and classifiers we refer to Kartaltepe et al. (2012). According to the CANDELS visual classification, sources are defined as 'disturbed' if at least 2/3 of the classifiers identified them as such, 'interacting' if the interaction metric (IM) is 0.2<IM<0.5 and 'mergers' if IM≥0.5 (see Rosario et al. 2015). We find an agreement of 86 per cent between our classification and the CANDELS visual classification of the same sources in GH-S; we therefore consider our disturbance assessment of the full IR quasar sample as reliable.

In Fig. 6, we plot the fraction of IR quasar host galaxies belonging to each of the three disturbance groups described above (disturbed, undisturbed and companion). We separated the unobscured/moderately obscured sources (green) and the heavily obscured sources (magenta; see Section 4.2). The 1σ errors in the plot are calculated following Gehrels (1986). The total fraction of IR quasars residing in undisturbed galaxies is ≈60 per cent, while that of the sources in disturbed/interacting systems is ≈40 per cent. These fractions are in good agreement with those found by Kocevski et al. (2012) for samples of AGN (≈56 per cent undisturbed and ≈44 per cent disturbed) and non-AGN hosting galaxies (≈52 per cent undisturbed and ≈48 per cent disturbed) at similar redshifts to our sample. This is true also for the fraction of sources showing a close companion (≈12 per cent). Separating the sources between heavily obscured and unobscured/moderately obscured quasars, we find suggestive evidence that the large majority of the unobscured quasars reside in undisturbed galaxies (≈80 per cent, as opposed to ≈47 per cent for the heavily obscured quasars), with only ≈20 per cent having visible signs of interactions; this fraction seems to be higher (≈53 per cent) amongst the heavily obscured quasars. Consistent results were found for a sample of X-ray-selected heavily obscured AGN in the COSMOS field by Lanzuisi et al. (2015). The drop in the number of disturbed galaxies amongst the

[9] The CANDELS visual classification is an ongoing programme currently including morphological and disturbance classifications for all the galaxies with $H < 24.5$ mag in the GOODS-S and UDS fields, and will soon provide classifications in all the remaining CANDELS fields. In their catalogue every source is inspected by at least 5 classifiers who assigned a number to each source as a measure of their disturbance and interaction/merger level (or 'interaction metric', IM).

unobscured/moderately obscured quasars might partly be due to the fact that the bright unobscured nucleus might impair the detection of faint signs of interactions, such as tidal features; we note that particular care has been applied to the classification of these sources to minimize this possible bias. Although the errors on the fractions of disturbed and undisturbed galaxies are relatively large, we find that the difference between unobscured/moderately obscured quasars and heavily obscured quasars is significant at 90 per cent confidence level (Fisher exact probability test, $P = 0.087$). However, larger samples are necessary to reliably assess these differences at higher confidence levels.

5 DISCUSSION

We have investigated the X-ray properties of a sample of 33 MIR selected quasars with intrinsic AGN luminosity $\nu L_{6\,\mu m} > 6 \times 10^{44}$ erg s^{-1} at redshift $z \approx 1$–3. While at MIR wavelengths these quasars are very luminous, the majority have low X-ray luminosities, and a significant fraction of them (∼30 per cent) are undetected in the deep *Chandra* data available in the GH fields, suggesting they are heavily obscured in the X-ray band. Indeed, the X-ray spectral analysis and the comparison between the X-ray and MIR luminosities indicate that the vast majority of these IR quasars are obscured (up to ∼79 per cent, 26 out of 33 sources), of which a large fraction are candidates to be CT (up to ∼48 per cent, i.e. 16 out of 33 quasars). The fractions of obscured and potentially CT quasars are much higher than those typically found for optically and X-ray-selected quasar samples (see Section 5.1). We have reliably identified eight of these sources as CT from the X-ray spectral analyses (N_H and strong Fe K α line), although some ambiguity still remains for three of them (XIDs 171N, 307N and 423N) due to the large uncertainties on the estimated N_H, from the suppression of the X-ray luminosity (a factor of ≈30–1000) compared to the 6 μm luminosity derived from the SED analyses and from the optical emission line luminosity. Further diagnostics are needed for the remaining eight CT quasar candidates to confirm their nature. Eight of our CT quasar candidates have also been classified as CT (or CT candidates) in previous studies (see Table 4, for reference), however, the remainders have never been identified to date. Our results therefore indicate that there is a large population of obscured and heavily obscured quasars at $z \approx 2$ and confirm that the selection of sources in the MIR band allows us to find even the most obscured, CT quasars, that are missing in the optical and X-ray bands.

5.1 Obscured quasar fraction: comparison with previous studies

Several studies conducted in the optical and X-ray bands have shown that the fraction of obscured AGN decreases with luminosity (e.g. Lawrence & Elvis 1982; Steffen et al. 2003; Ueda et al. 2003, 2014; Hasinger 2004, 2008; La Franca et al. 2005; Simpson 2005; Treister & Urry 2005). For instance, Hasinger (2008) found that the obscured fraction (f_{Cthin}), defined as the number of obscured, Compton-thin AGN (Cthin; N_H=10^{22}–10^{24} cm^{-2}) over the total with N_H<10^{24} cm^{-2}, amongst quasars is more than a factor of 2 lower (f_{Cthin} <25 per cent at $L_X > 10^{44}$ erg s^{-1}) than that for the less-powerful AGN (f_{Cthin} ≈50 per cent at $L_X = 10^{43}$ erg s^{-1}). This trend is also seen when selection biases are accounted for (due to the fact that unobscured bright quasars are easier to detect out to larger comoving volumes, e.g. Della Ceca et al. 2008). The obscured AGN fraction seems also to evolve with redshift, becoming larger at high redshift (e.g. La Franca et al. 2005; Ballantyne, Everett & Murray 2006; Treister & Urry 2006; Hasinger 2008; Ueda et al. 2014). The trend of decreasing f_{Cthin} at high luminosity, however, is found at all redshifts (e.g. Hasinger 2008; Ueda et al. 2014).

To compare the obscured fraction in our sample with those found in previous studies we consider here the Compton-thin quasars only, i.e. excluding sources with N_H>10^{24} cm^{-2}. Amongst our IR quasars $f_{Cthin} = 59$–72 per cent, where the range is determined by the lower and upper limit on the number of candidate CT quasars in our sample. These fractions are higher than those found by Hasinger (2008) for X-ray and optically-selected $L_X \approx 10^{44}$ erg s^{-1} quasars at $z = 1$–3, $f_{Cthin} \approx 40$–55 per cent. However, we find good agreement with the Ueda et al. (2014) estimates in the same redshift range, $f_{Cthin} \approx 60$–65 per cent at $L_X \approx 10^{44}$ erg s^{-1}, where they apply a correction for detection biases to the observed X-ray absorbed AGN fraction.

Taking into account the CT sources in our sample the obscured quasar fraction reaches ≈79 per cent (see Section 4.2), with CT quasars being up to ∼62 per cent of the total obscured quasars. This fraction is consistent with those found for Seyfert galaxies (L_X < 10^{44} erg s^{-1}) in the local Universe, where ∼50 per cent of the AGN population shows CT absorption (e.g. Risaliti, Maiolino & Salvati 1999; Guainazzi, Matt & Perola 2005; Tozzi et al. 2006), possibly suggesting that the relative ratio of Cthin and CT sources remains constant across all redshifts and luminosities. Our results also support the assumptions of the CXB synthesis models by Gilli et al. (2007) and Ueda et al. (2014) of an equal number of Cthin and CT AGN across all luminosities and redshifts. However, we note that different population synthesis models (e.g. Ballantyne et al. 2006; Treister et al. 2009) use different assumptions on the relative numbers of Cthin and CT AGN (see table 6 of Ueda et al. 2014). Buchner et al. (2015) found that obscured AGN (N_H>10^{22} cm^{-2}) at $\log L_X > 43.2$ erg s^{-1} contribute ≈75 per cent of the luminosity density at $z = 1$–3, with CT AGN and obscured Cthin AGN contributing in equal fractions, while unobscured AGN only making up ≈25 per cent of the luminosity density. We found consistent results for quasars ($L_X > 10^{44}$ erg s^{-1}).

In the context of galaxy evolution, where the most massive galaxies, hosts of the most luminous quasars, form earlier and evolve more rapidly than the less luminous systems (cosmic 'downsizing', e.g. Cowie et al. 1996; Franceschini et al. 1999), a decreasing fraction of obscured sources with luminosity can be explained with the most luminous AGN being more efficient than their less luminous analogues in consuming their surrounding gas and blowing off their dusty cocoon (through AGN feedback; e.g. Hopkins et al. 2006; Menci et al. 2008) becoming unobscured, bright quasars. This means that the probability of seeing obscured high-luminosity quasars is smaller than for lower luminosity AGN, as the fast accreting SMBHs spend a shorter time in this 'obscured phase'. However, at high redshifts we might expect to see more of these bright obscured quasars as they have not yet expelled or consumed all their surrounding material. Indeed, Assef et al. (2015) found that the space density of very luminous obscured quasars at high redshift ($2 < z < 4$) is comparable to that of unobscured quasars of similar luminosities. In this scenario it is perhaps not surprising to find such a high fraction of obscured quasars (∼80 per cent, including CT sources) in our sample at $z \approx 2$. In fact, there is indication that CT AGN have a similar evolution with redshift to Cthin AGN (e.g. Brightman & Ueda 2012; but see also Buchner et al. 2015). The selection in the IR band tends to find the most obscured, CT AGN more efficiently than in the optical and X-ray bands, and previous studies of MIR-selected AGN have indeed found high fractions of obscured and CT sources, consistent with our results (e.g. Maiolino

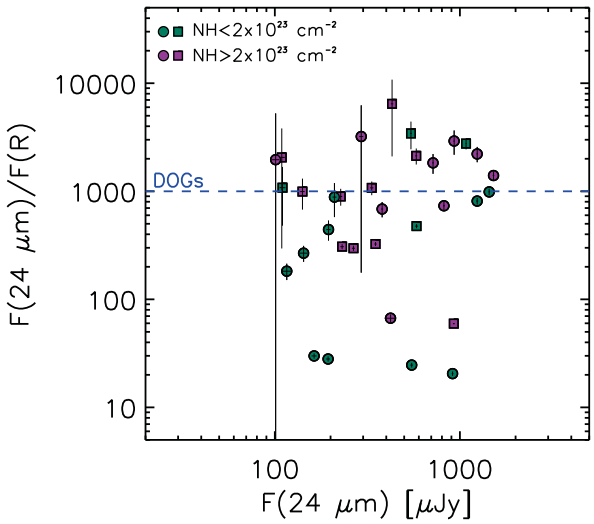

Figure 7. MIR-to-optical flux ratio, F(24 μm)/F(R), versus the *Spitzer* 24 μm flux density in units of μJy for our IR quasar sample. The sources in GH-N are shown as circles and the sources in GH-S as squares; heavily obscured quasars are represented in magenta, while the moderately obscured/unobscured quasars are in green (as in Fig. 3). The dashed line marks the flux ratio defining dust obscured galaxies (DOGs, F(24 μm)/F(R) > 1000; e.g. Fiore et al. 2008). The fraction of IR quasars in our sample that can be classified as DOGs is 39^{+24}_{-22} per cent.

et al. 2007; Fiore et al. 2008; Treister, Krolik & Dullemond 2008; Georgantopoulos et al. 2011a; Stern et al. 2014).

5.2 Comparison with the dust obscured galaxy population

X-ray obscured AGN have often been found to show extreme MIR-to-optical colours (F(24 μm)/F(R); where F(24 μm) is the flux density at 24 μm (observed frame) and F(R) is the flux density in the *R* band), due to strong reddening typically affecting the optical bands (e.g. Fiore et al. 2009; Georgantopoulos et al. 2009). Fiore et al. (2008) identified an MIR-to-optical colour selection, F(24 μm)/F(R) > 1000, as an efficient way to select heavily obscured, CT AGN, finding a large fraction (≈80 per cent) of such sources in their sample. Objects with these extreme MIR-to-optical colours have often been called dust obscured galaxies (DOGs; e.g. Dey et al. 2008; Pope et al. 2008b).

To investigate how our IR quasar selection, and our obscured quasar fraction compare to the DOG population, we plot the flux density ratio F(24 μm)/F(R) versus the flux density at 24 μm for all our IR quasars (Fig. 7). The *R* fluxes for the GH-N sources were derived from the Subaru Suprime-Cam *R*-band magnitudes (Capak et al. 2004), while for the GH-S sources they are extrapolated from the *HST*-ACS *v* and *i*-band magnitudes (Giavalisco et al. 2004). We find that a relatively small fraction of 39^{+24}_{-22} per cent [the errors on the fraction are estimated from the errors in the F(24 μm)/F(R) ratio and Poisson uncertainty] of our IR quasars show the extreme colours typical of DOGs. The fraction of heavily obscured quasars amongst them (10/13 sources; ≈77 per cent) is in good agreement with that found by Fiore et al. (2008). Of these sources, eight are amongst our CT quasar candidates (see Table 4). However, almost half of the quasars that we identified as heavily obscured in our sample would be missed by the DOG colour selection (9/19; ≈47 per cent), including ≈50 per cent of our CT quasar candidates (8/16 sources).[10] This indicates that the DOG colour selection is highly incomplete in identifying CT quasars and, even though some of the most heavily obscured quasars are likely to have extreme F(24 μm)/F(R) colours, this is not true for all of them. Indeed, as discussed in Section 3.2, the colour selections can be strongly affected by contamination from the host galaxy emission and by the *k*-correction, as the source redshift is not accounted for in these methods, and therefore cannot provide a clean and complete selection of quasars. For our quasars, we do not find any significant relation between the F(24 μm)/F(R) ratio and the redshift or the SFRs; further investigation on which of these effects have the biggest impact on the DOG colour selection, however, is beyond the scopes of this paper.

5.3 Space density of CT quasars

Considering the full IR quasar sample, we calculate the sky density of our sources ($\nu L_{6\,\mu m} > 6 \times 10^{44}$ erg s^{-1} at $z = 1$–3) within the GH fields (North and South; ∼260 arcmin^2 in total) to be ≈460 deg^{-2}. CT quasars constitute up to ≈48 per cent of our sources, i.e. up to ≈62 per cent of the obscured quasars in our sample (26 objects with $N_H > 10^{22}$ cm^{-2}). Calculating the space density of CT quasars (and CT candidates) in our sample (∼8–16 sources) in the comoving volume between $z = 1$–3 we find $\Phi = (6.7 \pm 2.2) \times 10^{-6}$ Mpc^{-3}, where the errors are estimated from the lower and upper limits on the number of CT quasars in our sample.

In Fig. 8, we plot the comoving CT quasar space density estimated in this work and compare it with those found in previous studies. Our results are consistent with the space density of $L_X = 10^{44}$–10^{45} erg s^{-1} (intrinsic) CT quasars at $z \approx 1.2$–2.2 found by Fiore et al. (2009), who based their estimates on IR selected sources in the COSMOS field. Alexander et al. (2008) calculated the volume density of CT quasars at $z \approx 2$–2.5 in the CDF-N based on four sources identified in the X-ray and IR bands; their estimate is somewhat higher than ours, but it is in broad agreement given their large uncertainties. Our estimate is in good agreement with the CT quasars space density predicted by the Gilli et al. (2007) model for intrinsic $L_X > 10^{44}$ erg s^{-1} at $z \approx 2$ and also with the values found by Tozzi et al. (2006) and Brightman & Ueda (2012), from X-ray spectral analyses in the CDF-S (Fig. 8).

For a more direct comparison with the X-ray studies of Tozzi et al. (2006) and Brightman & Ueda (2012), we limit our sample here to the CT quasars (and candidates) identified in the GH-S field (eight sources, three of which are detected in the X-rays). The space density estimated by Tozzi et al. (2006) for CT AGN at $z \approx 2$, is based upon four CT AGN identified from X-ray spectral analysis in the central 95 arcmin^2 in CDF-S (1 Ms). Brightman & Ueda (2012) identified ∼10 CT AGN in the CDF-S (≈460 arcmin^2) at $z \approx 1$–3 and intrinsic $L_X > 10^{44}$ erg s^{-1}, yielding a similar volume density to Tozzi et al. (2006) and to ours. However, it is important to note that there is no overlap between the CT AGN identified by Tozzi et al. (2006) and those identified in this work through spectral analysis (i.e. the three X-ray-detected sources in GH-S). Two of our three X-ray-detected CT quasars were undetected in the 1 Ms *Chandra* observations analysed in Tozzi et al. (2006), while the third source was mis-classified as a low-luminosity, unobscured AGN. On the

[10] We note that the optical and near-IR photometry of the source #6 (XID 243N) is contaminated by a nearby low-*z* galaxy (see also note in Table 1), and therefore its F(24 μm)/F(R) ratio, which results to be well below the DOG selection threshold, might not be reliable.

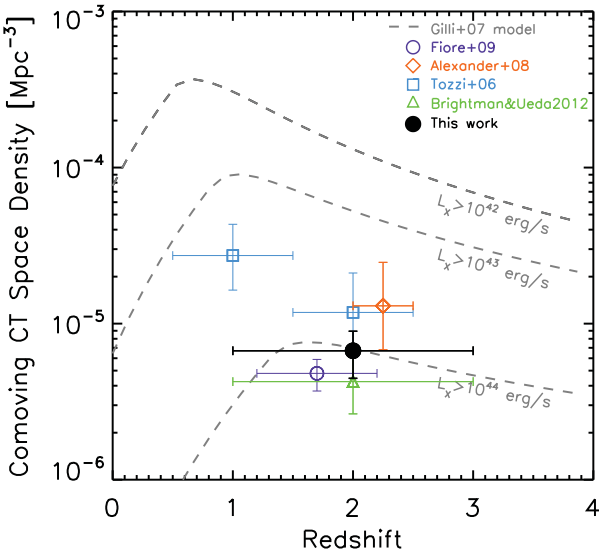

Figure 8. Space density of CT quasars at redshift $z = 1$–3 estimated from our IR quasar sample within the GH fields (black circle). The grey dashed lines are the space density predictions from the Gilli et al. (2007) model for AGN with $L_X > 10^{44}$ erg s^{-1}, $L_X > 10^{43}$ erg s^{-1} and $L_X > 10^{42}$ erg s^{-1} (from bottom to top). Results from various previous studies are also shown: the space density of quasars with $L_X > 10^{44}$ erg s^{-1} at $z \approx 2$ from Brightman & Ueda (2012, green triangle), Fiore et al. (2009, purple circle), Alexander et al. (2008, orange diamond) and Tozzi et al. (2006, blue squares). We also show the space density of AGN with $L_X > 10^{43}$ erg s^{-1} at $z \approx 1$ from Tozzi et al. (2006).

other hand, all the CT AGN identified by Tozzi et al. (2006) have lower MIR AGN luminosity than our IR quasars (although still consistent with the scatter of the L_X–$L_{6\,\mu m}$ relation), and therefore are not selected in our sample, as we are only probing the most luminous IR quasars. Two out of the three X-ray-detected CT quasars, we identified in the GH-S field were also classified as CT by Brightman & Ueda (2012), using the same *Chandra* data as in this work; the third source was not included in the Brightman & Ueda (2012) sample, but was analysed by Brightman et al. (2014) and classified as a CT quasar. Nevertheless, the overlap between our CT quasar candidates and those found by Brightman & Ueda (2012) is small (≈20–25 per cent, only two sources), as most of our CT candidates are X-ray undetected, while the CT quasars (with intrinsic $L_X > 10^{44}$ erg s^{-1}) identified by Brightman & Ueda (2012) have MIR AGN luminosities below our IR quasar threshold (according to our SED analyses). This is perhaps just a selection effect due to the scatter of the L_X–$L_{6\,\mu m}$ relation; however, it might also suggest that the quasar selection approaches in the MIR and X-ray bands are complementary, and tend to identify different source populations (e.g. Brightman & Ueda 2012), where the MIR selected CT quasars are brighter at MIR wavelengths and more obscured (e.g. $N_H \gtrsim$ (5–10) $\times$ 10^{24} cm^{-2}, as the majority are X-ray undetected) than the X-ray-selected CT quasars, possibly because of a larger dust content in the circumnuclear regions. If we combine the number of CT quasars identified in our work over the GH-S field with those found by Brightman & Ueda (2012) within the same area (∼7 sources within the GH-S area, of which two are in common with ours), we would obtain a total CT quasar space density of $\Phi = (1.9 \pm 0.6) \times 10^{-5}$ Mpc^{-3}. This is in agreement with the predictions by Shi et al. (2013) based on a joint model of the X-ray and IR backgrounds. This suggests that the best estimate of the true space density of CT quasars is possibly obtained from a combination of the CT populations identified in the IR and in the X-ray bands.

5.4 IR quasars and BH-galaxy co-evolution

According to some evolution scenarios, the most luminous AGN, hosted in the most massive systems, experience a different evolutionary path than that of smaller, less luminous systems. Major mergers are predicted to play a significant role in driving gas into the centre of the most massive galaxies, causing violent episodes of starbursts and rapid SMBH growth (e.g. Di Matteo et al. 2005; Hopkins et al. 2006), especially at high redshifts (e.g. Hopkins, Kocevski & Bundy 2014). On the other hand, secular processes, such as disc instabilities and galaxy bars, are expected to be the main mechanisms driving the gas into the centre of smaller, low-luminosity systems, where the SMBH and the galaxy experience a slower and more steady growth (see also Alexander & Hickox 2012, for a review). To place the IR quasars, which are the brightest MIR sources detected in the GH fields, into this evolution scenario, we investigated the host galaxy properties in terms of the SFR and the level of disturbance in the galaxy morphology to detect signs of possible recent interactions/mergers. Our quasars have typically SFRs consistent with those of MS SFGs at redshift $z \approx 1$–3, with no indication of unobscured quasars having suppressed SF (i.e. below the star-forming MS) compared to the most obscured ones (Fig. 4). We note, however, that amongst the three quasars with the highest SFRs within our sample (SFR≈800 $M_\odot$yr^{-1}), two are CT quasars, one of which is X-ray undetected (#1), and the remainder is heavily obscured by $N_H \approx 5 \times 10^{23}$ cm^{-2}. This suggests that in these sources large amounts of cold gas over the whole galaxy might be partly responsible for the obscuration. However, we do not find any direct correlation between the SFRs and N_H over the whole sample, suggesting that in general the X-ray obscuration is probably confined to the nuclear regions and not related to the gas on galaxy scales (e.g. Rosario et al. 2012; Rovilos et al. 2012).

As the morphology of the majority of our sources does not show any strong distortion features (∼60 per cent), we can infer that mergers are not the main fuelling process amongst the IR quasars (Fig. 6). This is in good agreement with the merger/interaction fractions found in less luminous AGN and non-AGN hosting galaxies at similar redshifts by Kocevski et al. (2012), but it is in contrast with the evolution scenario proposed for quasars (e.g. Di Matteo et al. 2005; Hopkins et al. 2006). However the fraction of disturbed/interacting systems (∼40 per cent) is on average higher than those found for sources at lower redshifts (≈15–20 per cent at $z < 1$; e.g. Cisternas et al. 2011), in agreement with the observed increase of the galaxy merger rate with redshift (e.g. Conselice et al. 2003; Kartaltepe et al. 2007).

Interestingly, the fraction of unobscured/moderately obscured quasars hosted in disturbed systems is significantly lower (≈20 per cent) than those in undisturbed galaxies (≈80 per cent; see Fig. 6), while the heavily obscured quasars are equally found in disturbed and undisturbed galaxies, suggesting that the merger fraction in the most heavily obscured systems might be higher (see also Kocevski et al. 2015). The difference between the two quasar populations is significant at the 90 per cent confidence level ($P = 0.087$, see Section 4.4). If unobscured quasars represent a later stage of the SMBH-galaxy evolution compared to the heavily obscured quasars, the distortion/interaction features due to mergers or galaxy interactions might have faded by the time these quasars are observed as unobscured, as the relaxation time of the galaxy is typically ∼200–400 Myr (e.g. Lotz et al. 2010). This might

explain the smaller fraction of disturbed systems we found for the unobscured/moderately obscured quasars. On the other hand, the most heavily obscured quasars might still be at a younger stage of evolution after the merger, and therefore their hosts still show the signatures of the recent interactions. We note, however, that we did not find any direct connection between the SFR and X-ray obscuration in our quasars, and thus no evidence for an enhancement of SFR in the heavily obscured quasars in disturbed systems, challenging the predictions from the quasar evolution scenarios. However, as the size of our sample is small, we cannot derive any strong conclusion from our results. Further analyses of larger quasar samples and comparisons with well selected control samples of galaxies are needed to accurately test the SMBH-galaxy evolution scenarios.

6 SUMMARY AND CONCLUSIONS

Through detailed SED decomposition analyses of the 24 μm-detected sources in the GH-N and GH-S fields we identified a sample of 33 luminous IR quasars with AGN MIR luminosity $\nu L_{6\,\mu m} > 6 \times 10^{44}$ erg s^{-1} at redshift $z \approx 1$–3. Considering typical intrinsic $L_X - L_{6\,\mu m}$ relations, this luminosity corresponds to an intrinsic X-ray luminosity of $L_{2-10\,keV} > 2 \times 10^{44}$ erg s^{-1}, i.e. in the quasar regime. We investigated the X-ray properties of these IR quasars through X-ray spectral analysis for the X-ray-detected sources to accurately derive the obscured quasar fraction and constrain the CT quasar population at $z \approx 2$. Through our SED analyses, which provide reliable measurements of the intrinsic AGN luminosity and of the host galaxy SFR, and through visual classification of the galaxy disturbance morphology using high-resolution *HST* images, we also investigated the host galaxy properties in relation to the quasar luminosity and the X-ray obscuration to understand the SMBH-galaxy connection in the context of the evolution scenarios. Our main results can be summarized as follows.

(1) X-ray spectral analyses of the X-ray-detected IR quasars (∼70 per cent of the sample) show that the majority of the sources (16 out of 24) are obscured by column densities $N_H > 10^{22}$ cm^{-2}, with more than half of them (9/16) being heavily obscured ($N_H > 2 \times 10^{23}$ cm^{-2}). Given that the fraction of obscured AGN decreases at high luminosity (Section 5.1), the number of obscured quasars in our sample is high; however, we find it is consistent with those expected from an increase of the obscured fraction with redshift (after accounting for detection biases, e.g. Ueda et al. 2014).

(2) Despite being the brightest quasars at MIR wavelengths detected in the GH fields, about 30 per cent of our IR quasars are not detected in the deepest 2 and 4 Ms *Chandra* X-ray data. Their X-ray luminosity upper limits imply a suppression of the X-ray emission by factors of ∼30–1000 compared to the intrinsic MIR AGN luminosity. From the comparison of the MIR and observed X-ray luminosities for all the IR quasars in our sample, we constrain the fraction of CT quasars to be ≈24–48 per cent (8–16 quasars, six of which are robustly identified through X-ray spectral analyses), i.e. up to ∼62 per cent of all the obscured quasars in the sample (Section 4.2).

(3) The space density of CT quasars at $z = 1$–3 estimated from our sample is $\Phi = (6.7 \pm 2.2) \times 10^{-6}$ Mpc^{-3}, which is in general agreement with previous results for quasars identified in the X-ray or MIR bands (Tozzi et al. 2006; Alexander et al. 2008; Fiore et al. 2009; Brightman & Ueda 2012) as well as with the predictions from the population synthesis models (e.g. Gilli et al. 2007). However, the small overlap between the CT quasars identified through our analyses and those found in the X-rays within the same fields (e.g. Brightman & Ueda 2012) suggests that the space density of CT quasars is likely to be higher than that estimated in this work (or those found in previous studies based on X-ray-detected sources), and that the combination of X-ray and MIR-selected CT populations possibly provides the best constraints on their true space density in the Universe (Section 5.3).

(4) The SFRs of the IR quasar hosting galaxies are broadly consistent with those of MS galaxies at $z \approx 1$–3. In general, we do not find any direct correlation between the SFR and the quasar luminosity or with the X-ray obscuration, with only tentative indication for the heavily obscured quasars ($N_H > 2 \times 10^{23}$ cm^{-2}) to have higher SFRs than the less obscured ones (in particular at $z = 1.5$–2.5). The limited number of sources in our sample, however, does not allow us to derive any strong conclusion from this result (Section 4.3).

(5) From visual classification of the galaxy morphology to identify signs of interactions/mergers we find that ≈40 per cent of our quasars have a disturbed morphology, while ≈60 per cent do not show any sign of distortions, indicating that mergers are not the main mechanism fuelling the SMBH in luminous quasars. This is consistent with the results found for lower luminosity AGN (e.g. Kocevski et al. 2012). However, the interaction/merger fraction seems to be lower for unobscured/moderately obscured quasars than for heavily obscured quasars, possibly suggesting that large amounts of gas and dust in the galaxy, as a result of recent merger or galaxy interactions, are partly responsible for the high level of obscuration in these quasars, while the unobscured/moderately obscured quasars might be at a later evolutionary stage, where the signatures of galaxy interactions/mergers have already faded (Section 4.4).

Further progress can be made in the near future to constrain the CT quasar population using the extremely deep 7 Ms *Chandra* data recently obtained in the CDF-S (PI: W. Brandt). These data will allow us to confirm the CT nature of the CT quasar candidates we identified in the GH-S field (e.g. providing better spectra and detecting some of the X-ray-undetected systems), further validating our analyses and results. Moreover, the advent of the new X-ray and MIR observatories, such as *eROSITA*, *ATHENA* and the *James Webb Space Telescope (JWST)* will provide unprecedentedly large samples of high-z quasars to allow studies of MIR- and X-ray-selected CT quasars, placing tighter constraints of their space density and on the different properties characterizing sources selected in the MIR versus those selected in the X-ray bands.

ACKNOWLEDGEMENTS

We thank the anonymous referee for the useful comments and suggestions that helped improving the manuscript. We gratefully acknowledge financial support from the Science and Technology Facilities Council (STFC, ST/L00075X/1; ADM, DMA and CMH) and the Leverhulme Trust (DMA). FEB acknowledges support from CONICYT-Chile (Basal-CATA PFB-06/2007, FONDECYT 1141218, Gemini-CONICYT 32120003, 'EMBIGGEN' Anillo ACT1101), and the Ministry of Economy, Development, and Tourism's Millennium Science Initiative through grant IC120009, awarded to The Millennium Institute of Astrophysics, MAS. WNB acknowledges the Chandra X-ray Center grant G04-15130A and NASA ADP grant NNX10AC99G. YQX acknowledges support of the Thousand Young Talents program (KJ2030220004), the 973 Program (2015CB857004), the USTC startup funding (ZC9850290195), the NSFC-11473026, NSFC-11421303, the Strategic Priority Research Program 'The Emergence of

Cosmological Structures' of the Chinese Academy of Sciences (XDB09000000) and the Fundamental Research Funds for the Central Universities (WK3440000001).

REFERENCES

Adams J. J. et al., 2011, ApJS, 192, 5
Alexander D. M., Hickox R. C., 2012, New Astron. Rev., 56, 93
Alexander D. M. et al., 2003, AJ, 126, 539
Alexander D. M. et al., 2008, ApJ, 687, 835
Arnaud K. A., 1996, in Jacoby G., Barnes J., eds, ASP Conf. Ser. Vol. 101, Astronomical Data Analysis Software and Systems V. Astron. Soc. Pac., San Francisco, p. 17
Assef R. J. et al., 2015, ApJ, 804, 27
Balestra I. et al., 2010, A&A, 512, A12
Ballantyne D. R., Everett J. E., Murray N., 2006, ApJ, 639, 740
Barger A. J. et al., 2003, AJ, 126, 632
Blackburn J. K., 1995, in Shaw R. A., Payne H. E., Hayes J. J. E., eds, ASP Conf. Ser. Vol. 77, Astronomical Data Analysis Software and Systems IV. Astron. Soc. Pac., San Francisco, p. 367
Brandt W. N., Alexander D. M., 2015, A&AR, 23, 1
Brightman M., Nandra K., 2011, MNRAS, 413, 1206
Brightman M., Ueda Y., 2012, MNRAS, 423, 702
Brightman M., Nandra K., Salvato M., Hsu L.-T., Aird J., Rangel C., 2014, MNRAS, 443, 1999
Broos P. S., Townsley L. K., Feigelson E. D., Getman K. V., Bauer F. E., Garmire G. P., 2010, ApJ, 714, 1582
Broos P., Townsley L., Getman K., Bauer F., 2012, Astrophys. Source Code Library, ascl.1203.001
Buchner J. et al., 2014, A&A, 564, A125
Buchner J. et al., 2015, ApJ, 802, 89
Capak P. et al., 2004, AJ, 127, 180
Cash W., 1979, ApJ, 228, 939
Chen C.-T. J. et al., 2015, ApJ, 802, 50
Cisternas M. et al., 2011, ApJ, 726, 57
Comastri A., Setti G., Zamorani G., Hasinger G., 1995, A&A, 296, 1
Conselice C. J., Bershady M. A., Dickinson M., Papovich C., 2003, AJ, 126, 1183
Cowie L. L., Songaila A., Hu E. M., Cohen J. G., 1996, AJ, 112, 839
Daddi E. et al., 2004, ApJ, 600, L127
Del Moro A. et al., 2013, A&A, 549, A59 (DM13)
Del Moro A. et al., 2014, ApJ, 786, 16
Della Ceca R. et al., 2008, A&A, 487, 119
Dey A. et al., 2008, ApJ, 677, 943
Di Matteo T., Springel V., Hernquist L., 2005, Nature, 433, 604
Dickey J. M., Lockman F. J., 1990, ARA&A, 28, 215
Donley J. L., Rieke G. H., Pérez-González P. G., Barro G., 2008, ApJ, 687, 111
Donley J. L. et al., 2012, ApJ, 748, 142
Draine B. T., 2003, ARA&A, 41, 241
Elbaz D. et al., 2011, A&A, 533, A119
Fabian A. C., Iwasawa K., Reynolds C. S., Young A. J., 2000, PASP, 112, 1145
Fazio G. G. et al., 2004, ApJS, 154, 10
Ferrarese L., Merritt D., 2000, ApJ, 539, L9
Feruglio C., Daddi E., Fiore F., Alexander D. M., Piconcelli E., Malacaria C., 2011, ApJ, 729, L4
Fiore F. et al., 2008, ApJ, 672, 94
Fiore F. et al., 2009, ApJ, 693, 447
Franceschini A., Hasinger G., Miyaji T., Malquori D., 1999, MNRAS, 310, L5
Fruscione A. et al., 2006, Proc. SPIE, 6270, 62701V
Gallagher S. C., Hines D. C., Blaylock M., Priddey R. S., Brandt W. N., Egami E. E., 2007, ApJ, 665, 157
Gandhi P., Horst H., Smette A., Hönig S., Comastri A., Gilli R., Vignali C., Duschl W., 2009, A&A, 502, 457
Gandhi P. et al., 2014, ApJ, 792, 117
Gehrels N., 1986, ApJ, 303, 336
Georgantopoulos I., Akylas A., Georgakakis A., Rowan-Robinson M., 2009, A&A, 507, 747
Georgantopoulos I., Rovilos E., Xilouris E. M., Comastri A., Akylas A., 2011a, A&A, 526, A86
Georgantopoulos I. et al., 2011b, A&A, 531, A116
Giavalisco M. et al., 2004, ApJ, 600, L93
Gierliński M., Done C., 2004, MNRAS, 349, L7
Gilli R., Comastri A., Hasinger G., 2007, A&A, 463, 79
Griffin M. J. et al., 2010, A&A, 518, L3
Grogin N. A. et al., 2011, ApJS, 197, 35
Guainazzi M., Matt G., Perola G. C., 2005, A&A, 444, 119
Harrison C. M. et al., 2012, ApJ, 760, L15
Hasinger G., 2004, Nucl. Phys. B, 132, 86
Hasinger G., 2008, A&A, 490, 905
Hopkins P. F., Hernquist L., Cox T. J., Di Matteo T., Robertson B., Springel V., 2006, ApJS, 163, 1
Hopkins P. F., Kocevski D. D., Bundy K., 2014, MNRAS, 445, 823
Kartaltepe J. S. et al., 2007, ApJS, 172, 320
Kartaltepe J. S. et al., 2012, ApJ, 757, 23
Kass R. E., Raftery A. E., 1995, J. Am. Stat. Assoc., 90, 773
Kennicutt R. C., Jr, 1998, ARA&A, 36, 189
Kirkpatrick A. et al., 2012, ApJ, 759, 139
Kocevski D. D. et al., 2012, ApJ, 744, 148
Kocevski D. D. et al., 2015, ApJ, 814, 104
Koekemoer A. M. et al., 2011, ApJS, 197, 36
Kormendy J., Ho L. C., 2013, ARA&A, 51, 511
La Franca F. et al., 2005, ApJ, 635, 864
Lacy M. et al., 2004, ApJS, 154, 166
Lacy M., Sajina A., Petric A. O., Seymour N., Canalizo G., Ridgway S. E., Armus L., Storrie-Lombardi L. J., 2007, ApJ, 669, L61
Lansbury G. B. et al., 2014, ApJ, 785, 17
Lansbury G. B. et al., 2015, ApJ, 809, 115
Lanzuisi G. et al., 2015, A&A, 573, A137
Lawrence A., Elvis M., 1982, ApJ, 256, 410
Le Fèvre O. et al., 2004, A&A, 428, 1043
Lehmer B. D., Alexander D. M., Bauer F. E., Brandt W. N., Goulding A. D., Jenkins L. P., Ptak A., Roberts T. P., 2010, ApJ, 724, 559
Lotz J. M., Jonsson P., Cox T. J., Primack J. R., 2010, MNRAS, 404, 575
Luo B. et al., 2008, ApJS, 179, 19
Luo B. et al., 2014, ApJ, 794, 70
Lutz D., Maiolino R., Spoon H. W. W., Moorwood A. F. M., 2004, A&A, 418, 465
Lutz D. et al., 2010, ApJ, 712, 1287
Madau P., Ferguson H. C., Dickinson M. E., Giavalisco M., Steidel C. C., Fruchter A., 1996, MNRAS, 283, 1388
Magdziarz P., Zdziarski A. A., 1995, MNRAS, 273, 837
Magnelli B., Elbaz D., Chary R. R., Dickinson M., Le Borgne D., Frayer D. T., Willmer C. N. A., 2009, A&A, 496, 57
Magnelli B., Elbaz D., Chary R. R., Dickinson M., Le Borgne D., Frayer D. T., Willmer C. N. A., 2011, A&A, 528, A35
Magorrian J. et al., 1998, AJ, 115, 2285
Mainieri V., Bergeron J., Hasinger G., Lehmann I., Rosati P., Schmidt M., Szokoly G., Della Ceca R., 2002, A&A, 393, 425
Maiolino R., Shemmer O., Imanishi M., Netzer H., Oliva E., Lutz D., Sturm E., 2007, A&A, 468, 979
Marconi A., Hunt L. K., 2003, ApJ, 589, L21
Mateos S., Barcons X., Carrera F. J., Ceballos M. T., Hasinger G., Lehmann I., Fabian A. C., Streblyanska A., 2005, A&A, 444, 79
Mateos S. et al., 2008, A&A, 492, 51
Mateos S., Alonso-Herrero A., Carrera F. J., Blain A., Severgnini P., Caccianiga A., Ruiz A., 2013, MNRAS, 434, 941
Mateos S. et al., 2015, MNRAS, 449, 1422
Menci N., Fiore F., Puccetti S., Cavaliere A., 2008, ApJ, 686, 219
Mignoli M. et al., 2005, A&A, 437, 883
Mulchaey J. S., Koratkar A., Ward M. J., Wilson A. S., Whittle M., Antonucci R. R. J., Kinney A. L., Hurt T., 1994, ApJ, 436, 586

Mullaney J. R., Alexander D. M., Goulding A. D., Hickox R. C., 2011, MNRAS, 414, 1082
Mullaney J. R. et al., 2012, MNRAS, 419, 95
Murphy E. J., Chary R.-R., Alexander D. M., Dickinson M., Magnelli B., Morrison G., Pope A., Teplitz H. I., 2009, ApJ, 698, 1380
Nandra K., Pounds K. A., 1994, MNRAS, 268, 405
Netzer H., Mainieri V., Rosati P., Trakhtenbrot B., 2006, A&A, 453, 525
Oliver S. J. et al., 2012, MNRAS, 424, 1614
Poglitsch A. et al., 2008, Proc. SPIE, 7010, 701005
Pope A. et al., 2008a, ApJ, 675, 1171
Pope A. et al., 2008b, ApJ, 689, 127
Popesso P. et al., 2009, A&A, 494, 443
Pounds K. A., Reeves J. N., 2009, MNRAS, 397, 249
Richards G. T. et al., 2006, ApJS, 166, 470
Rieke G. H. et al., 2004, ApJS, 154, 25
Risaliti G., Maiolino R., Salvati M., 1999, ApJ, 522, 157
Rosario D. J. et al., 2012, A&A, 545, A45
Rosario D. J. et al., 2015, A&A, 573, A85
Rovilos E. et al., 2012, A&A, 546, A58
Rovilos E. et al., 2014, MNRAS, 438, 494
Salpeter E. E., 1955, ApJ, 121, 161
Sanders D. B., Soifer B. T., Elias J. H., Madore B. F., Matthews K., Neugebauer G., Scoville N. Z., 1988, ApJ, 325, 74
Schwarz G., 1978, Ann. Stat., 6, 461
Shi Y., Helou G., Armus L., 2013, ApJ, 777, 6
Silverman J. D. et al., 2010, ApJS, 191, 124
Simpson C., 2005, MNRAS, 360, 565
Spergel D. N. et al., 2003, ApJS, 148, 175
Stanley F., Harrison C. M., Alexander D. M., Swinbank A. M., Aird J. A., Del Moro A., Hickox R. C., Mullaney J. R., 2015, MNRAS, 453, 591
Steffen A. T., Barger A. J., Cowie L. L., Mushotzky R. F., Yang Y., 2003, ApJ, 596, L23
Steidel C. C., Hunt M. P., Shapley A. E., Adelberger K. L., Pettini M., Dickinson M., Giavalisco M., 2002, ApJ, 576, 653
Stern D., 2015, ApJ, 807, 129
Stern D. et al., 2005, ApJ, 631, 163
Stern D. et al., 2014, ApJ, 794, 102
Szokoly G. P. et al., 2004, ApJS, 155, 271
Tombesi F., Cappi M., Reeves J. N., Palumbo G. G. C., Yaqoob T., Braito V., Dadina M., 2010, A&A, 521, A57
Tozzi P. et al., 2006, A&A, 451, 457
Treister E., Urry C. M., 2005, ApJ, 630, 115
Treister E., Urry C. M., 2006, ApJ, 652, L79
Treister E., Krolik J. H., Dullemond C., 2008, ApJ, 679, 140
Treister E., Urry C. M., Virani S., 2009, ApJ, 696, 110
Trouille L., Barger A. J., Cowie L. L., Yang Y., Mushotzky R. F., 2008, ApJS, 179, 1
Turner T. J., George I. M., Nandra K., Mushotzky R. F., 1997, ApJ, 488, 164
Ueda Y., Akiyama M., Ohta K., Miyaji T., 2003, ApJ, 598, 886
Ueda Y. et al., 2007, ApJ, 664, L79
Ueda Y., Akiyama M., Hasinger G., Miyaji T., Watson M. G., 2014, ApJ, 786, 104
Vanzella E. et al., 2008, A&A, 478, 83
Xia L. et al., 2011, AJ, 141, 64
Xue Y. Q. et al., 2011, ApJS, 195, 10
Xue Y. Q. et al., 2012, ApJ, 758, 129
Yaqoob T., 1997, ApJ, 479, 184
Young S., Axon D. J., Robinson A., Hough J. H., Smith J. E., 2007, Nature, 450, 74

APPENDIX A: INFRARED SEDS OF THE IR QUASARS

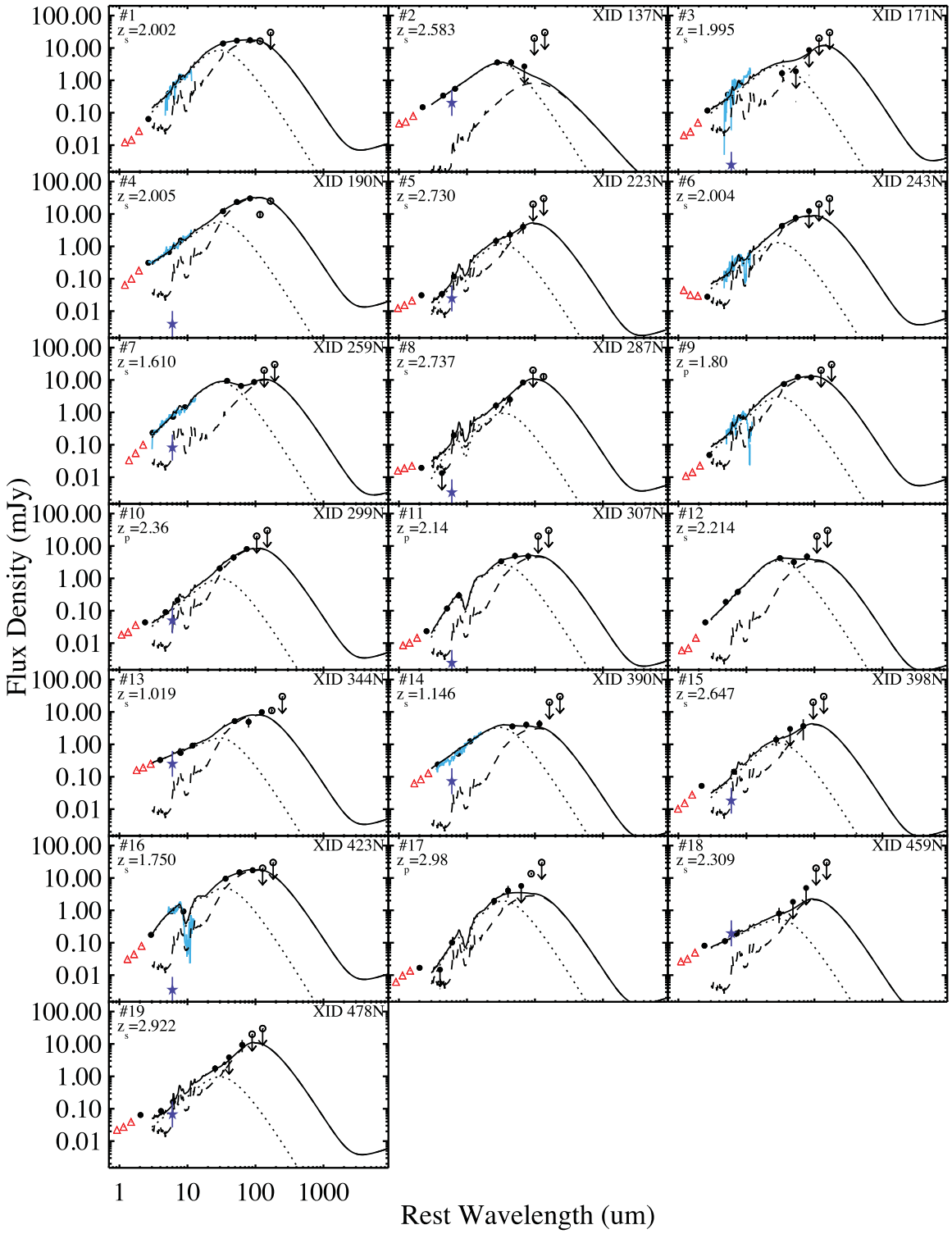

Figure A1. SED of the IR quasars in GH-N. Filled circles are the *Spitzer* 8.0, 16 and 24 μm and *Herschel* 100, 160 and 250 μm data used to constrain the SEDs. The *Spitzer*-IRAC 3.6, 4.5 and 5.8 μm data (open triangles) and the *Herschel* 350 and 500 μm (open circles) are also shown, although these data are not used in the SED-fitting process (Section 3.1). For 8 out of 19 IR quasars in GH-N (∼42 per cent) *Spitzer*-IRS spectra are available and they are shown here (cyan line) to demonstrate the agreement with the best-fitting SEDs. The dotted curves and the dashed curves represent the AGN and SFG templates, respectively, while the solid curve is the total best-fitting SED. The purple stars, which are only shown for the X-ray-detected IR quasars, represent the 6 μm flux we would expect from the observed X-ray luminosity adopting the Lutz et al. (2004) relation (for XID 243N the star falls below the plotted flux range). On the top-left corner of each plot we report the source number and the redshift, while on the top-right corner there is the XID from Alexander et al. (2003) for the X-ray-detected quasars.

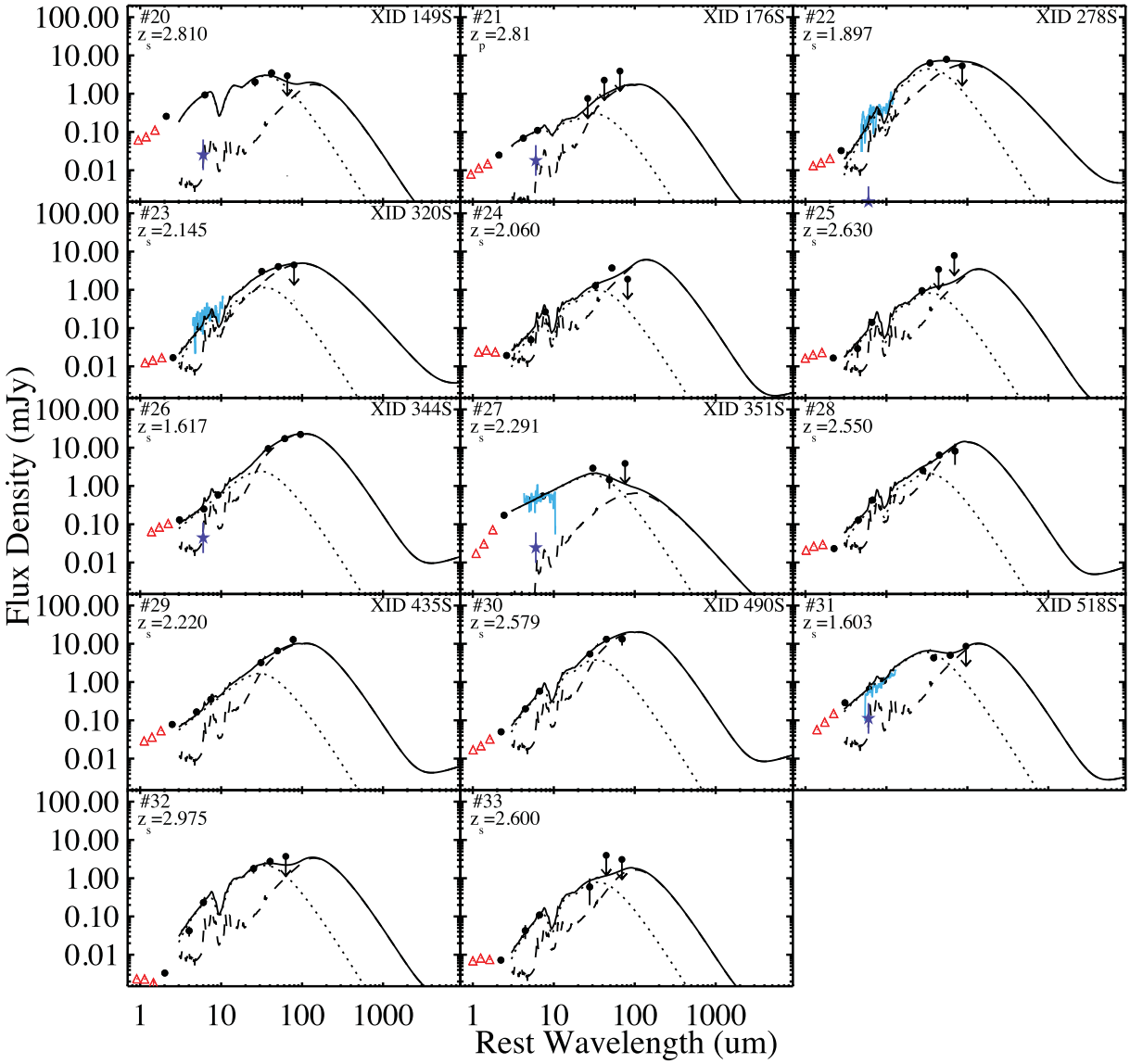

Figure A2. SED of the IR quasars in GH-S. Symbols are the same as in Fig. A1. The *Spitzer*-IRS spectra, which are available for 4 out of the 14 IR quasars in GH-S (∼29 per cent) are shown (cyan lines) to demonstrate the agreement with the best-fitting SEDs. For XIDs 320S, 435S and 490S, which we robustly identified as CT quasars, the purple stars, which represent the 6 μm flux we would expect from the observed X-ray luminosity adopting the Lutz et al. (2004) relation, falls below the plotted flux range. On the top-left corner of each plot we report the source number and the redshift, while on the top-right corner there is the XID from Xue et al. (2011) for the X-ray-detected quasars.

This paper has been typeset from a TEX/LATEX file prepared by the author.